

Louisiana Tech University

Louisiana Tech Digital Commons

Doctoral Dissertations

Graduate School

Summer 8-2022

Dynamics of a Charge Carrier Driven by Oscillating Fields in Materials with Impurities

Dileon Saint-Jean

Louisiana Tech University

Follow this and additional works at: <https://digitalcommons.latech.edu/dissertations>

Recommended Citation

Saint-Jean, Dileon, "" (2022). *Dissertation*. 980.

<https://digitalcommons.latech.edu/dissertations/980>

This Dissertation is brought to you for free and open access by the Graduate School at Louisiana Tech Digital Commons. It has been accepted for inclusion in Doctoral Dissertations by an authorized administrator of Louisiana Tech Digital Commons. For more information, please contact digitalcommons@latech.edu.

**DYNAMICS OF A CHARGE CARRIER DRIVEN BY
OSCILLATING FIELDS IN MATERIALS
WITH IMPURITIES**

by

Dileon Saint-Jean, B.Sc., M.S.

A Dissertation Presented in Partial Fulfillment
of the Requirements for the Degree
Doctor of Philosophy: Computational Analysis & Modeling

COLLEGE OF ENGINEERING AND SCIENCE
LOUISIANA TECH UNIVERSITY

August 2022

LOUISIANA TECH UNIVERSITY

GRADUATE SCHOOL

June 29, 2022

Date of dissertation defense

We hereby recommend that the dissertation prepared by

Dileon Saint-Jean, B.Sc., M.S.

entitled **Dynamics of a Charge Carrier Driven by Oscillating Fields in Materials
with Impurities**

be accepted in partial fulfillment of the requirements for the degree of

Doctor of Philosophy in Computational Analysis & Modeling

Pedro Derosa

Pedro Derosa

Supervisor of Dissertation Research

Weizhong Dai

Weizhong Dai

Head of Computational Analysis & Modeling

Doctoral Committee Members:

Mary Fendley
Bassiby Dembele
Pradeep Chowriappa
Markus Wobisch

Approved:

Hisham Hegab

Hisham Hegab
Dean of Engineering & Science

Approved:

Ramu Ramachandran

Ramu Ramachandran
Dean of the Graduate School

ABSTRACT

In conductive materials and semiconductors, a charge carrier under the effects of an electric field will suffer collisions due to thermal fluctuations and impurities in the lattice, altering their trajectory. The electronic properties of these materials depend on the nature and frequency of these collisions; thus, they must be accounted for in any model dealing with electrical conduction. Tracking all collisions individually, while it may be possible within certain limits, forces the model to a large degree of approximation. This work introduces a Monte Carlo-based methodology to electrical transport in Ohmic materials that consists of two parts, the utilization of probability distribution functions (PDFs) for a set of collisions (coarse grain), as opposed to solving the transport equations for individual collisions and the use of homotopies to parameterize PDFs what produces a continuous set of PDFs once a relatively small number of them are explicitly parameterized. With the current approach, simulation times are from a few hundred to a few thousand times smaller than explicitly solving the transport equations. Average collision times are generated from distributions for a set of n collisions (the grain size), and from there, transport properties are calculated. Simulations were used to solve equations of motion based on the Drude's Model of electrical conductivity. The results of the simulations are then used to generate probability distributions for various combinations of input parameters in order to coarse-grain the transport model. Grain sizes of $n=5$ and $n=50$ were considered. A homotopy on start time was first created by evaluating select distribution parameters across a half cycle. An excellent agreement non-coarse grained model was obtained.

The electric field was then incorporated into the model parameterization leading to a PDF that, via a homotopy, can generate average collision time for any initial position of the carrier under any electric field within a continuous range). Results were validated using the non-coarse grained simulation under conditions not used for the parametrization for up to 500,000 collisions, with current density values being above 98.9% accurate. The goal of this work was to build a homotopy or mapping that, given some input parameters, could output some transport properties to aid experimental studies. The material of choice for this work was an ideal ohmic conductor with a mean free path of 4.3×10^{-9} m.

APPROVAL FOR SCHOLARLY DISSEMINATION

The author grants to the Prescott Memorial Library of Louisiana Tech University the right to reproduce, by appropriate methods, upon request, any or all portions of this Dissertation. It is understood that “proper request” consists of the agreement, on the part of the requesting party, that said reproduction is for his personal use and that subsequent reproduction will not occur without written approval of the author of this Dissertation. Further, any portions of the Dissertation used in books, papers, and other works must be appropriately referenced to this Dissertation.

Finally, the author of this Dissertation reserves the right to publish freely, in the literature, at any time, any or all portions of this Dissertation.

Author _____

Date _____

DEDICATION

For my family.

TABLE OF CONTENTS

| | |
|---|-----|
| ABSTRACT..... | iii |
| APPROVAL FOR SCHOLARLY DISSEMINATION | v |
| DEDICATION | vi |
| LIST OF TABLES | ix |
| LIST OF FIGURES | xi |
| ACKNOWLEDGMENTS | xiv |
| CHAPTER 1 INTRODUCTION | 1 |
| 1.1 Background..... | 1 |
| 1.2 About This Work | 5 |
| CHAPTER 2 GENERAL METHODOLOGY..... | 7 |
| 2.1 Introduction..... | 7 |
| 2.1.1 Monte Carlo Methods | 7 |
| 2.1.2 Boltzmann Transport Theory..... | 9 |
| 2.1.3 Drude’s Model | 11 |
| 2.2 Charge Transport Model and Algorithm..... | 16 |
| 2.2.1 General Charge Transport Model Based on the Drude’s Model | 16 |
| 2.2.2 Charge Transport Model | 18 |
| 2.3 Coarse Graining Methodology..... | 23 |

| | |
|---|----|
| CHAPTER 3 HOMOTOPY ON START TIME | 26 |
| 3.1 Homotopy Theory | 26 |
| 3.2 Preliminaries to a Homotopy on Start Time | 27 |
| 3.3 Homotopy on Start Time | 34 |
| 3.3.1 Grain Size of $n=5$ | 34 |
| 3.3.2 Grain Size of $n=50$ | 46 |
| 3.3.3 Effect of Grain Size on Current Density | 52 |
| CHAPTER 4 HOMOTOPY ON START TIME AND ELECTRIC FIELD | 56 |
| 4.1 Homotopy in Two Dimensions | 56 |
| 4.1.1 Evaluation of Effects of the Electric Field | 56 |
| 4.1.2 2-D Homotopy Construction | 59 |
| 4.2 Model Validation | 68 |
| CHAPTER 5 OTHER TECHNIQUES AND METHODS | 75 |
| 5.1 Homotopy on Position | 75 |
| 5.2 Homotopy on Frequency | 79 |
| CHAPTER 6 CONCLUSIONS AND FUTURE WORK | 81 |
| 6.1 Conclusions | 81 |
| 6.2 Future Work | 82 |
| REFERENCES | 84 |

LIST OF TABLES

| | |
|---|----|
| Table 2-1: <i>Simulation Input Parameters</i> | 21 |
| Table 3-1: <i>Simulation Input Parameters</i> | 29 |
| Table 3-2: <i>PDF Parameter Estimates for Different Numbers of Events</i> | 30 |
| Table 3-3: <i>Similarity of Histogram Data for Time to 1 Event</i> | 32 |
| Table 3-4: <i>Simulation Time for Individual Collisions and a Coarse-Grained Model</i> | 34 |
| Table 3-5: <i>Summary of Simulation Start Times and Corresponding Positions (+ and - Indicate the Direction of Movement)</i> | 35 |
| Table 3-6: <i>Simulation Input Parameters</i> | 39 |
| Table 3-7: <i>Homotopy on Start Time Parameters</i> | 41 |
| Table 3-8: <i>Individual Collisions (IC) and Coarse-Grained (CG) Model Average Collision Time (τ) for Select Total Events</i> | 44 |
| Table 3-9: <i>Individual Collisions (IC) and Coarse-Grained (CG) Model Peak Current Density (J_{rms}) for Select Total Events</i> | 45 |
| Table 3-10: <i>Homotopy on Start Time Coefficients</i> | 47 |
| Table 3-11: <i>Individual Collisions (IC) and Coarse-Grained (CG) Model Average Collision Time (τ) for Select Total Events</i> | 51 |
| Table 3-12: <i>Individual Collisions (IC) and Coarse-Grained (CG) Model Current Density (J_{rms}) for Select Total Events</i> | 52 |
| Table 3-13: <i>Individual Collisions (IC) and Coarse-Grained (CG) Models Current Density (J_{rms}) for 500,000 Collisions</i> | 54 |
| Table 3-14: <i>Individual Collisions (IC) and Coarse-Grained (CG) Model Average Collision Time (τ) for 500,000 Collisions</i> | 54 |

| | |
|--|----|
| Table 4-1: <i>Comparison of Average Collision Time (τ) for Various Electric Field Amplitudes after 1 Event</i> | 58 |
| Table 4-2: <i>Simulation Input Parameters for 2-D homotopy</i> | 62 |
| Table 4-3: <i>Two-Dimensional Homotopy Coefficients for μ_2, σ_2 and ζ between $L(E_0) \leq t \leq U(E_0)$</i> | 62 |
| Table 4-4: <i>Two-Dimensional Homotopy Coefficients for μ</i> | 63 |
| Table 4-5: <i>Two-Dimensional Homotopy Coefficients for σ_1</i> | 64 |
| Table 4-6: <i>Individual Collisions (IC) and Coarse-Grained (CG) Model Average Collision Time (τ) for 500 and 20000 Events, $E_0=55$ N/C</i> | 68 |
| Table 4-7: <i>Individual Collisions and Coarse-Grained Models' Current Density (J_{rms}) for 500 and 20000 Events, $E_0=55$ N/C</i> | 68 |
| Table 4-8: <i>Comparison of Simulation Output for 2-D Homotopy Average Collision Time for Individual Collisions (IC) and Coarse-Grained (CG) Model</i> | 69 |
| Table 4-9: <i>Comparison of Simulation Output for 2-D Homotopy Peak Current Density</i> | 69 |
| Table 5-1: <i>Parameter Estimates and Similarity for Varying Repetitions Event Sizes</i> | 77 |
| Table 5-2: <i>Parameter Estimates and Similarity for Varying Repetitions Event Sizes</i> | 79 |

LIST OF FIGURES

| | |
|---|----|
| Figure 2-1: Charge carrier in a periodic electric field with no collisions showing Acceleration and Velocity (a) and Position (b)..... | 18 |
| Figure 2-2: Charge carrier in a periodic electric field with multiple collisions..... | 22 |
| Figure 2-3: Charge transport model algorithm | 22 |
| Figure 3-1: Comparison of distributions with varying total number of events (m) describing time data a) 100 events b) 1,000 events c) 10,000 events d) 100,000 events .. | 28 |
| Figure 3-2: Comparison of distributions with varying total number of events (n) describing time data a) 100 events b) 1,000 events c) 10,000 events d) 100,000 events with original simulation data overlaid | 31 |
| Figure 3-3: Comparison of individual collision simulation time and coarse-grained times for generation of various numbers of events (m) | 33 |
| Figure 3-4: Comparison of select start times and eventual stopping times after one event..... | 36 |
| Figure 3-5: Comparison of select start times and parameters describing distributions of total flight time after one event..... | 37 |
| Figure 3-6: Histogram of data with time offset near $\frac{1}{4}$ of a cycle..... | 39 |
| Figure 3-7: Homotopy on start time for 100 events showing total flight time a) and Current Density b)..... | 42 |
| Figure 3-8: Homotopy on start time for 1,000 events showing total flight time a) and Current Density b)..... | 42 |
| Figure 3-9: Homotopy on start time for 10,000 events showing total flight time a) and Current Density b)..... | 43 |
| Figure 3-10: Homotopy on start time for 50,000 events showing total flight time a) and Current Density b)..... | 43 |

| | |
|--|----|
| Figure 3-11: Homotopy on start time for 100,000 events showing total flight time a) and Current Density b)..... | 44 |
| Figure 3-12: Comparison of select start times and parameters describing distributions of total flight time after $n=50$ collisions (1 event)..... | 46 |
| Figure 3-13: Homotopy on start time for 10 events showing total flight time a) and Current Density b)..... | 48 |
| Figure 3-14: Homotopy on start time for 100 events showing total flight time a) and Current Density b)..... | 49 |
| Figure 3-15: Homotopy on start time for 1,000 events showing total flight time a) and Current Density b)..... | 49 |
| Figure 3-16: Homotopy on start time for 5,000 events showing total flight time a) and Current Density b)..... | 50 |
| Figure 3-17: Homotopy on start time for 10,000 events showing total flight time a) and Current Density b)..... | 50 |
| Figure 3-18: Comparison of total flight time of source simulation against homotopy with $n=5$ and $n=50$ | 53 |
| Figure 3-19: Current density compared across individual collisions, and homotopy of $n=5$ and $n=50$ | 54 |
| Figure 3-20: Comparison of total flight time of source simulation against homotopy with $n=5$ and $n=50$ – Finer View | 55 |
| Figure 4-1: Parameter estimates for mean (μ) across electric fields and start times | 57 |
| Figure 4-2: Total flight time of individual Collisions against Coarse Grained Model on electric fields and start times with $m=500$ events, $E=55$ N/C | 66 |
| Figure 4-3: Current Density of individual Collisions against Coarse Grained Model on electric fields and start times with $m=500$ events, $E=55$ N/C | 66 |
| Figure 4-4: Total flight time when individual Collisions are considered against Coarse Grained Model on electric fields and start times with $m=20,000$ events, $E=55$ N/C..... | 67 |
| Figure 4-5: Current Density of individual Collisions against Coarse Grained Model on electric fields and start times with $m=20,000$ events, $E_0 =55$ N/C | 67 |

| | |
|--|----|
| Figure 4-6: Total Flight Time of individual Collisions against Coarse Grained Model on electric fields and start times with $m=20,000$ events, $E=30$ N/C | 70 |
| Figure 4-7: Current density of individual Collisions against Coarse Grained Model on electric fields and start times with $m=20,000$ events, $E=30$ N/C | 70 |
| Figure 4-8: Total Flight time of individual Collisions against Coarse Grained Model on electric fields and start times with $m=20,000$ events, $E=60$ N/C | 71 |
| Figure 4-9: Current density of individual Collisions against Coarse Grained Model on electric fields and start times with $m=20,000$ events, $E=60$ N/C | 71 |
| Figure 4-10: Total Flight time of individual Collisions against Coarse Grained Model on electric fields and start times with $m=100,000$ events, $E=30$ N/C | 72 |
| Figure 4-11: Current density of individual Collisions against Coarse Grained Model on electric fields and start times with $m=100,000$ events, $E=30$ N/C | 72 |
| Figure 4-12: Current density of individual Collisions against Coarse Grained Model on electric fields and start times with $m=1000$ events, $E_0=5$ N/C | 73 |
| Figure 4-13: Total Flight Time of individual Collisions against Coarse Grained Model on electric fields and start times with $m=1000$ events, $E_0=5$ N/C | 74 |
| Figure 5-1: Comparison of distributions with varying total number of events (m) describing position data a) 100 events b) 1,000 events c) 10,000 events d) 100,000 events | 77 |
| Figure 5-2: Comparison of parameter fit with varying total number of events (m) describing position data a) 100 events b) 1,000 events c) 10,000 events d) 100,000 events | 77 |
| Figure 5-3: Comparison of fit generated from varying total number of events (m) describing position data a) 100 events b) 1,000 events c) 10,000 events d) 100,000 events | 78 |
| Figure 5-4: Mean position after one event with varied Electric Field and Frequency | 80 |

ACKNOWLEDGMENTS

The author would like to acknowledge their main research supervisor for this work, Dr. Pedro Derosa, for guidance and direction throughout this process. He has guided and supported me throughout all aspects of my doctoral education and research. In addition, the supervisory committee members, Dr. Pradeep Chowriappa, Dr. Bassidy Dembele, Dr. Mary Fendley, and Dr. Markus Wobisch, are all thanked for their advice on this project.

The author would also like to thank their family and friends for their unwavering support, my wife Shonice Saint-Jean, my siblings Dinah Lorde, Dwight Piper, and Dirk Saint-Jean, and Delana Saint-Jean, who supported me, my parents Petter and Jemma Saint-Jean who pushed me to complete this endeavor and my home church, the La Plaine Pentecostal Church, whose prayers sustained me.

Valuable computation resources provided by the Louisiana Optical Network Initiative (LONI) are graciously acknowledged as they were used exclusively.

CHAPTER 1

INTRODUCTION

1.1 Background

As society advances to a more connected state, more and more devices are being developed. These connected devices require detailed investigation prior to fabrication, with demand expected to exceed supply in the coming years [1]–[4]. All of these components that are used in every device are built using semiconductors. From diodes to transistors and integrated circuits, they are built using semiconductors and have contributed almost half a trillion dollars to the global economy in 2020 alone [5].

Considering the importance of electronic components, it is essential to understand the characteristics of these materials and how they work in specific situations. 2021 also saw what was termed the “Global Chip Shortage” due in part to the coronavirus pandemic [6]–[10]. The supply chain issues the world experienced during this time exposed the vulnerability of dependence on foreign supply chains as well as previously underestimated trade friction and the potential knock-on effects on the semiconductor industry [11]–[14]. This occurrence has encouraged the government to invest in this important industry, with a recent report indicating that the US senate has approved over \$50 billion in subsidies for chip manufacturers [15] following the White House’s 100-day review of US supply chains [16]. This investment has the benefit of incentivizing additional research and development in this field.

With these developments, some advances will inevitably be made, whether in the fabrication of new materials, repurposing old ones, or finding new ways that they can be used. To fully embrace the opportunities that exploring new directions would bring, methods able to determine the connection between materials structure and its properties are needed as a means to assist in the design of new materials with desired properties. Many studies have investigated materials and their properties, such as conductance [17]–[19], resistivity [20], carrier mobility ([20]–[23]), and carrier concentration [23]–[25]. These studies typically model a known physical quantity and compare its prediction to experimental results, a very useful method that, however, can be somewhat limiting in the scope as a singular material is usually studied.

Charge transport mechanisms are different processes that account for different ways in which particles can move from one place to another. In order to study transport processes, theoretical models have been created and are employed to quantitatively describe different transport mechanisms, for example, and most relevant to this work, the flow of electric current through some medium. The most basic of these models leads to the Ohms law (Eq. 1-1); however, the actual transport mechanism depends on the microscopic nature of the material, and therefore, models that account for microscopic details and interactions can potentially be used to describe any transport regime.

$$I = \frac{V}{R} \quad \text{Eq. 1-1}$$

An understanding of how charge carriers traverse various materials is the first step required in the design and improvement of advanced devices. Charge carrier mobility is one of the fundamental properties of materials in general that determine their conduction properties. Carrier mobility has been extensively studied experimentally, addressing

specific situations [26]–[31]. The interest goes beyond traditional semiconductors; Luo et al., for example, examined the effects of enhancing carrier mobility in conjugated polymer field-effect thin-film transistors by utilizing tetramethylammonium oxide. Their experiments indicated a 24-fold increase in hole mobility compared to non-enhanced materials [32]. Other research by Meijer shows that carrier mobility can be reliably estimated experimentally [26], [31]. These experimental studies are useful in their own right; however, one downside is that experiments must investigate singular materials at a time. In that regard, transport models, on the other hand, can be specific to a given material or study a particular property for a generic material and can often be used to inform experimentalists on the best or most promising combinations to provide the best performance.

Multiple computational transport models have been developed over the last few decades. These models vary based on the underlying theoretical background upon which they are built as well as the physical phenomena that are modeled [19], [33]–[39]. A review of methods used in drift-diffusion models was provided by Jerome, which summarized many of the current methods used in charge transport and some specific analytic solutions [40]. Another publication by Jacoboni and Reggiani reviewed the Monte Carlo method for the solution of charge transport [36]. Monte Carlo methods are broadly described as a class of computational algorithms that use random sampling on a repeated basis to provide some approximation of a numerical result [41]. In their review, the authors provided a comprehensive model for the solution of charge transport in semiconductors using unidirectional and periodic electric fields and magnetic fields. The

authors also highlighted an algorithm for implementing said solution, which includes provisions for dealing with materials impurities via scattering/collision events.

Another review of modeling techniques of charge transport in semiconductors by Grondin et al. highlighted models that are particle-based, where the trajectories of individual particles are tracked using ensemble Monte Carlo techniques [42]. In these models, a random walk of an individual particle, subject to continuous acceleration and collisions, is simulated as a sequence of free flights. Each free flight is independent of the other and is terminated by some scattering event that is instantaneous. The ensemble Monte Carlo calculations attempt to find as close to an exact stochastic solution to the microscopic process. However, the transport accuracy depends on the accuracy of the model and the number of statistically independent paths that are simulated. Another class of models outlined is those that are energy-momentum conserving or hydrodynamic. These models are based on obtaining moments of the Boltzmann transport equation. This approach is not as computationally expensive as the ensemble Monte Carlo method previously described; however, its complexity lies in the fact that various parameters, such as the average collision time/ relaxation time, need to be known or obtained, often via Monte Carlo. In that regard, some way of minimizing the computational cost of Monte Carlo techniques is necessary.

Multiple methods exist for graining or coarse graining a process [43]–[46]. Broadly, coarse graining refers to reducing the granularity of a process to reduce the computational complexity. It is particularly useful in cases where Monte Carlo is involved. Many coarse graining methods will group like processes together [47] by analyzing how a group of processes functions, rather than each individual process. This

methodology inevitably has the drawback of a slightly reduced accuracy [48]; however, provided that said reduced accuracy is within acceptable bounds, these methods are invaluable in complexity reduction [49]. This approach has also been employed to simulate charge transport [50], [51], with different models being developed regularly. The goal of most of these coarse-grained models is to create a general-purpose model that, by graining a process, grouping together elements of the system or processes that are modeled as one unit, thus reducing the simulation time and the complexity of the system to be modeled. The work presented in this dissertation is similar in that regard. The primary difference is in the use of homotopies as a means for coarse graining.

The Chapter 3 discusses some of the important preliminary components that are central to this dissertation: Monte Carlo Methods, Boltzmann Transport Theory, and Drude's Model. In most cases, two classes of problems are solved using Monte Carlo methods: integration and optimization. For the purposes of this work, the methods discussed will primarily address the optimization class of problems. Drude's model of electrical conductance, a simplification of the problem of electron transport through conductors in both electric and magnetic fields, is also highlighted.

1.2 About This Work

This dissertation is organized as follows: Chapter 2 discusses the overall methodology of the model, while Chapter 3 outlines the basics of a coarse-grained charge transport model based on Drude's model for charge carriers in a single dimension. Potential routes to improve this model are outlined in Chapter 4 with details on various statistical methods for parameterization as well as various problems encountered during parameterization and potential solutions. Chapter 4 also outlines the results of a

coarse-grained charge transport model with a homotopy in electric field and start time.

Chapter 5 outlines some of the methods that were implemented but were not successful as a guide for future research. The conclusions and future work are discussed in Chapter 6.

CHAPTER 2

GENERAL METHODOLOGY

2.1 Introduction

Chapter 2 discusses some of the important preliminary components that are central to this dissertation: Monte Carlo Methods, Boltzmann Transport Theory, and Drude's Model. Monte Carlo methods are broadly described as a class of computational algorithms that use random sampling on a repeated basis to provide some approximation of a numerical result [41]. In most cases, two classes of problems are solved with these methods: integration and optimization. For the purposes of this work, the methods discussed will primarily address the optimization class of problems. The basic Boltzmann transport theory, which describes the statistical behavior of a thermodynamic system not in equilibrium, is briefly discussed. Drude's model of electrical conductance, a simplification of transport of electrons through conductors in electric fields, is also introduced, followed by the specifics of the transport model implemented in this work and the coarse-graining approach that is the core contribution of this dissertation.

2.1.1 Monte Carlo Methods

Monte Carlo methods rely on a sequence of random values that are generated with some given probabilities. The idea is to use randomness to simulate the solution of a real system. Monte Carlo Methods are based on Markov chains, where every step in a sequence is only correlated to the previous step. They are the go-to option when it is

either difficult or impossible to use other methods, and they are particularly helpful in optimization problems. For instance, Monte Carlo Methods can be used to more easily simulate physical systems that otherwise would be too difficult due to the number of variables, such as problems in fluid dynamics, strongly coupled solids, and interacting particle systems [41]. At each step, a random value is sorted based on an appropriate probability distribution that reflects the physics of a system.

One or more probability distributions are used. These distributions are where the physics of the problem is coded. A random sample is then generated using said distributions. That random sample is the output that follows the input distribution. Analysis of the output is then performed to determine the next step. The main idea behind this method is that because results are computed based on repeated random samples and statistical analysis, an averaged, unbiased result will be produced. By doing so, previously unknown parameters such as those of a distribution representing the flight time of a carrier, which can be difficult to find experimentally, can be determined. Due to the nature of Monte Carlo methods, each run is just one of a very large number of possible paths the system may follow. Therefore, a large number of histories must be simulated, and they can often take a lot of time to get to a reasonable approximation of the solution; as such, they may seem time-consuming. Most Monte Carlo algorithms are, however, embarrassingly parallelizable as one calculation is typically independent of the other. Massively parallel systems can therefore take advantage of this built-in parallelism advantage.

Monte Carlo methods are useful in solving multiple physical problems in computational physics. More relevant to the purpose of this work, they are useful in

providing solutions to electron charge transport problems [36], [41], [52]–[54]. Monte Carlo methods enable the simulation of complex physical phenomena that would not be possible or very hard to solve with conventional PDE analysis. Monte Carlo algorithms specifically geared at electron charge transport are semiclassical in nature and will generally yield a probabilistic solution to the Boltzmann transport equation. In this general, semiclassical approach, the trajectory of charge carriers is tracked. The trajectory is considered to consist of regions of free flight separated by scattering events that are chosen randomly [33].

An accurate solution to the carrier transport problem requires fore knowledge of the material under non-equilibrium conditions, such as the effect of a periodic electric field. Additionally, though many models exist, each applies under specific conditions and, in general, requires significant computational power to observe properties at the nanoscale. In general, Monte Carlo methods, when used to model charge transport in semiconductors, do so by simulating the motion of a charge carrier under the effects of some external force due to an applied electric or magnetic field. One assumption is that the motion of the carrier will be interrupted due to events, such as scattering caused by defects in the material. The duration of the carrier flight, distance traveled, or the state after a collision (event) is determined stochastically based on some given probabilities describing the process.

2.1.2 Boltzmann Transport Theory

The Boltzmann Transport Theory forms the basis for developing microscopic models for quantities such as mobility and conductivity [55]. It can be used to study transport of charge carriers in various materials, particularly in gases.

In the presence of external forces, the Boltzmann Transport Equation (BTE) applies (Eq. 2-1). Three main reasons account for a change in electron distribution:

1. The motion of the electron
2. The influence of external forces
3. Various scattering processes

The generalized BTE describes a system out of equilibrium due to the above-mentioned reasons. It arises by considering a probability distribution for the probability that a particle will be in a set position and has a particular momentum at a moment in time which depends on the Fermi-Dirac distribution [55]. This equation (Eq. 2-1) can be used to understand how physical quantities, such as energy and momentum, change when particles are in transport [56]. Other properties can be derived, including viscosity and electrical conductivity from these.

$$\left. \frac{\partial f}{\partial t} \right|_{coll} = \frac{\partial f}{\partial t} + \frac{\partial f}{\partial x} \cdot \frac{p}{m} + \frac{\partial f}{\partial p} \cdot F \quad \text{Eq. 2-1}$$

Eq. 2-1 shows the relation of how particles move, changing their position and momentum because of diffusion, external fields, and collisions. The function f represents the local concentration of electrons in a particular location. The first term evaluates how f changes with time. The second term on the right comes from the movement of particles, and the third is produced by particles drifting due to an external action such as a force. Exact analytical solutions of the Boltzmann equation exist in some specific cases. While these solutions can be insightful, they have limited practical use as they are available under very restricted assumptions which are not generally applicable to a wide range of applications [55]. Numerical methods, such as finite element methods (FEM), are used to find approximate solutions to different forms of the BTEs [57]. One limitation of using

FEM specifically and numerical methods broadly is that an approximate solution of the Boltzmann equation will be the result. Additionally, as it relates to FEM, continuity between the finite elements describing the geometry must be maintained; otherwise, solutions may be invalid [58]. Provided the geometry is properly defined, complex and irregular shapes are easily discretized. One area of interest is the calculation of electrical conductivity. Most applications of the solutions for electrical conductivity match in order of magnitude with the semiclassical result; thus, they are particularly useful and somewhat accurate. This dissertation does not use the BTE as a basis for charge transport model development; rather, it uses a simplification, which is outlined in the section below, the Drude Model, developed by Paul Drude [59]. This is sufficient for the main purpose of this work which is to propose a homotopy-based coarse graining approach.

2.1.3 Drude's Model

Drude's model is a simplification of the transport problem. Two of the main differences between the Drude Model and the more general Boltzmann Transport Equation is that carriers are assumed to move in straight lines, and charge carriers are non-interacting. The Drude model can also be considered a microscopic justification of Ohm's Law, the empirical observation of conductors, which states that voltage is proportional to current [59].

$$V = IR \quad \text{Eq. 2-2}$$

Since material properties are of interest, Eq. 2-2 can be rewritten in a manner that is independent of the conductor geometry by restating the terms in Ohm's Law in terms of their microscopic equivalents. Eq. 2-2 further devolves into its component parts as expressed in Eq. 2-3, with the implication of Eq. 2-4 that the applied electric field (E) is equal to the product of the resistivity (ρ) and current density (J). By using that $V = El$,

where E is the applied electric field and l the length of the conductor, $I = JA$, where J is the current density and A the cross-sectional area of the conductor, and that $R = \rho \frac{l}{A}$, Eq.

2-2 can be re-written as:

$$El = JA \rho \frac{l}{A} \quad \text{Eq. 2-3}$$

Where the geometrical characteristics of the conductor, A , and l cancel, making the equation independent of the geometry. Now using that the conductivity is given by $\sigma = 1/\rho$:

$$J = \sigma E \quad \text{Eq. 2-4}$$

The Drude model applies Boltzmann's kinetic theory of gases to electrons. The theory explains the electrical and electronic contribution to the thermal conductivity of metals. One of the core building blocks of Drude's Theory was that electrons could be described as a classical gas of particles. In the original theory, four assumptions are made [60]:

1. Between Collisions (that only include collisions with the lattice), the interaction of a given electron, both with the other electrons and with the ions, is neglected.
2. Collisions are instantaneous events that abruptly change the velocity of an electron.
3. Electrons experience collisions with a probability $1/\tau$ per unit time, where τ is the average collision time.
4. Electrons emerge from a collision with zero velocity.

Due to assumption 1, in the absence of an external electromagnetic field, electrons are assumed to move in straight lines. This is also known as the *free electron*

approximation [61]. The collisions in assumption 2 account for the interaction between electrons and the crystal, either with the regular lattice, due to thermal vibrations, or with impurities that create a distortion in the potential energy map the electron must navigate. The quantity τ is known by many names, including the *average collision time*, *relaxation time*, and *mean free time*. It is assumed to be independent of the position and velocity of the electron and dependent on the material density, the temperature, and the distribution of impurities.

Electrical conductivity is a fundamental property of interest when modeling charge transport in various materials; the relationship has been outlined in Eq. 2-4. The current density J is the current going through a cross-sectional area per unit of area, or in terms of microscopic magnitudes.

$$J = -nev \quad \text{Eq. 2-5}$$

Where n is the carrier density (or electrons per unit of volume), e is the absolute value of the electron charge, and the drift velocity is given by v . The minus sign accounts for the convention that current is positive in the direction positive carriers would move in an electric field (opposite to electrons). Note that in the absence of an electric field, electrons will move at random in all directions; therefore, in the absence of an applied electric field, v averages out to be zero, and there is no current. In the presence of a field E , the drift velocity and current density can be expressed as follows:

$$v_d = -\frac{eE\tau}{m} \quad \text{Eq. 2-6}$$

$$J = -nev_{avg} = \frac{ne^2\tau}{m} E \quad \text{Eq. 2-7}$$

Comparing with Eq. 2-4:

$$\sigma = \frac{ne^2\tau}{m} \quad \text{Eq. 2-8}$$

The equations above (Eq. 2-6 to Eq. 2-8) account for an electric field that is unidirectional, i.e., direct current. Many studies have studied conductivity under this condition both experimentally and via simulations [62]–[66]. Some experimental studies have investigated the characteristics of a charge carrier under the sole effects of a periodic electric field ([32], [67]–[70]). However, these studies are usually for a specific material as opposed to a generic model where a material is defined by variables that represent its properties. Here is where modeling has an advantage, as it is better suited to study materials at a more fundamental level where minimal changes in input can potentially lead to significant changes in output.

A Monte Carlo simulation can be used to model such phenomena in materials with impurities under the effects of a periodic electric field. A simulation will start when a carrier has been given some initial position and velocity (which could be zero); then, either the time of flight or distance traveled before a collision is determined stochastically. These options are equivalent, and for this dissertation, some initial position is given, and the time of flight is randomly selected. Further details of this specific method are shared in Section 2.1.

With an applied electric field that is periodic in nature, Eq. 2-4 to Eq. 2-8 can be redefined as follows.

$$J(\omega, t) = \sigma(\omega)E(\omega, t) \quad \text{Eq. 2-9}$$

$$E(\omega, t) = E_0 \cos(\omega t) \quad \text{Eq. 2-10}$$

$$\sigma(\omega) = \frac{\sigma_0}{1-i\omega\tau} = \frac{\sigma_0}{1+\omega^2\tau^2} + i\omega\tau \frac{\sigma_0}{1+\omega^2\tau^2} \quad \text{Eq. 2-11}$$

$$\sigma_0 = \frac{n e^2 \tau}{m} \quad \text{Eq. 2-12}$$

$$J(\omega, t) = \left(\frac{\sigma_0}{1+\omega^2\tau^2} + i\omega\tau \frac{\sigma_0}{1+\omega^2\tau^2} \right) E_0 \cos(\omega t) \quad \text{Eq. 2-13}$$

Where ω is the frequency of the electric field, note these equations provide the solution to the direct current case (unidirectional electric field) for $\omega = 0$. By considering only the real part of $J(\omega)$ the root mean square of the current density, the square root of the time average of the square of the current density, can be described via Eq. 2-14.

$$J_{rms}(\omega) = \frac{1}{\sqrt{2}} \frac{\sigma_0}{1 + \omega^2 \tau^2} \quad \text{Eq. 2-14}$$

Tracking this information for a large number of collisions can be computationally expensive. To address this challenge, collisions were grouped or coarse-grained, so an event is defined as a set of collisions. Probability distributions are generated to describe the state of the charge after this collective event. This grouping allowed for the transport characteristics previously highlighted, such as the average collision time and, subsequently, current density, to be generated from a probability distribution representing positions and time after n collisions as opposed to one collision at a time, therefore saving time. Using these distributions, material properties, such as conductance, can be easily derived. This model is coarse-grained via the use of a homotopy to generate appropriate PDF's. A homotopy at base is a mapping of two continuous functions where one can be morphed into the other. The mapping provides a continuous set of functions that are intermediate functions between the two used to generate the homotopy. Additional details on homotopies are provided in Chapter 3. In the implementation proposed here, rather than morphing one distribution into another, a continuous map is created that approximately matches a set of functions that have been explicitly parameterized. In this way, it is not necessary to generate parameters for every condition to be simulated.

The simulation algorithm is composed of two main components: a charge transport routine and a coarse graining routine. These simulations were performed on a

single HPC server, the Queen Bee 2 (QB2) cluster. The QB2 cluster is available through the Louisiana Optical Network Initiative (LONI) and was primarily used for running simulations in parallel. The QB2 cluster had a 1.5 Petaflop peak performance when introduced in 2014 and was ranked the 46th most powerful supercomputer in the world at the time. The cluster currently contains 380 compute nodes, each containing 20 Xeon processor cores and at least two NVIDIA Tesla K20X GPUs. The code was initially run using the MATLAB programming language; however, due to licensing issues, the code was ported over to python, which does not require a node-specific license. Components of the chebpy routine were also used, a branch of root-finding tools provided by chebfun [71].

2.2 Charge Transport Model and Algorithm

2.2.1 General Charge Transport Model Based on the Drude's Model

The solution of the equation of motion for a free, charged particle in an oscillatory field is simple; however, in real materials (e.g., conductors), charge carriers suffer collisions that alter their trajectory. The collisions occur due to thermal fluctuations and impurities in the lattice. These collisions can affect the material response; thus, a proper way to account for them is needed if a model is to track carriers in the materials. A complete model that considers interactions between charge carriers, the material, and other components can be developed. However, the scale of these models becomes increasingly complex and impractical to adequately model at the nanoscopic scale. To address this complexity, a simplification, the Drude's Model, which was proposed by Paul Drude in 1900, may be used. The premise is that by using classical mechanics, the material is treated as a fixed array in a collection of unbound electrons that collide

randomly. The carriers will release all their momentum in each collision, effectively resetting their speed to zero [60], and do not interact with each other.

Mathematically, this implies that the velocity (v) is re-set to $v = 0$ every time the carrier collides, and this can happen randomly, at any time t_0 in their cycle. One of two parameters is necessary to apply Drude's model: λ , the average distance that a particle travels between collisions or *mean free path*, and τ , the average time between collisions or *average collision time*. The use of either of these two statistically derived quantities allows a system to be modeled, and some derived quantity, such as the electrical conductivity σ , can be approximated.

This approach to simulating charge transport is not new. Jacoboni and Reggiani (1983) previously provided an outline for developing Monte Carlo (MC) methods for the solution of charge transport [36].

In general, the physical system will be defined via some input parameters, including values such as the electric field, mean free path, start time, frequency, and the total number of collisions. Once the system has been defined, initial conditions to the problem are set. These initial conditions determine how the carrier behaves at the start, while the behavior after a collision is determined by the scattering mechanism, such as in the Drude Model, where carriers give out all their momentum. Following this step, total flight time is evaluated, the state of the carrier is decided immediately before and after the collision event, and data is collected to generate estimators. To examine such properties at the nanoscopic level, one requires significant computing power. The specific transport model used in this dissertation is outlined in 2.2.2.

2.2.2 Charge Transport Model

A charged particle in a periodic electric field will slow down and speed up in response to the electric field, provided there are no collisions. It is essentially a particle bouncing back and forth indefinitely in a system at equilibrium. Figure 2-1: Charge carrier in a periodic electric field with no collisions showing acceleration and velocity (a) and position (b).

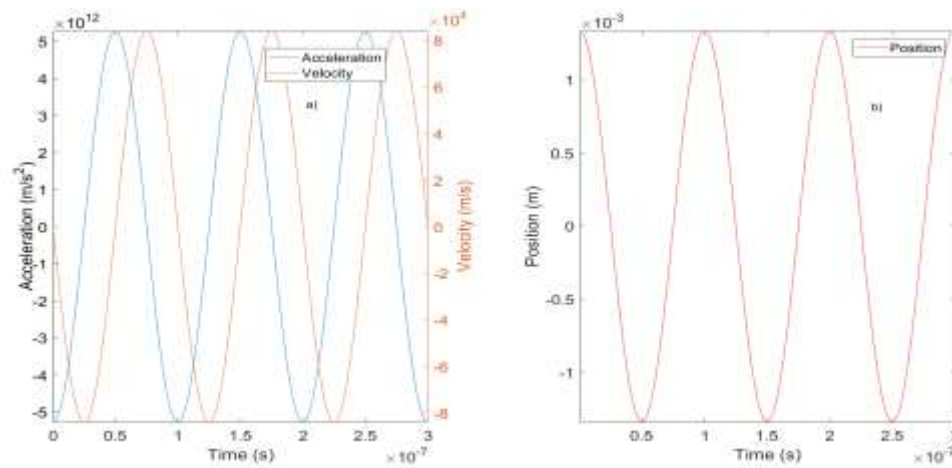


Figure 2-1: Charge carrier in a periodic electric field with no collisions showing acceleration and velocity (a) and position (b).

Such a system can be easily modeled; however, it would not represent most of the physical systems. The addition of collisions, required to resemble more closely the actual process, complicates the solutions, and MC methods may be more appropriate to use. To examine properties such as conductivity and average collision time at the nanoscopic level, one requires significant computing power [42].

Many studies have been conducted over the last decades that simulate charge transport in materials [63]–[66], though the majority of these evaluate the effects under a DC electric field. In particular, significant work has been done on charge transport in

specific materials such as carbon nanotubes, polyimide films, and polyethylene [42], [72]–[77], but not many studies have been reported discussing a more general solution.

Early studies have looked at charge transport in semiconductors [21], [28], [36], [53] and the associated MC methods that were employed to model these material properties. In MC models, it is usually assumed that particles do not interact with each other, and thus no particle-particle collisions exist. The typical process for these models is to apply a statistical approach to model the particle motion as a random walk of individual particles. The particles are subjected to an applied electric field and collisions with the media in which they are moving. Each “event” ends after a collision, with the procedure repeated multiple times. A review of charge transport modeling techniques by Grondin et al. indicates that such methods are computationally extremely expensive, considering the incredibly vast number of carrier interactions occurring at the nano scale [42].

When collisions are introduced, the prior equilibrium is broken, and this causes changes to material conductance and resistivity, two of the more commonly evaluated electrical properties. To understand this behavior, the effect of a periodic electric field on the electrical properties highlighted above needs to be evaluated. The following represents the relation between electric field strength and the force and Newton’s Second Law that provides the dynamic variables, starting with the acceleration.

$$\vec{E} = \frac{\vec{F}}{q} \quad \text{Eq. 2-15}$$

$$\vec{F} = m\vec{a} \quad \text{Eq. 2-16}$$

The electric field here is defined as $\vec{E} = E \cos(\omega t)$. By equating Eq. 2-15 and Eq. 2-16, the time-dependent acceleration representing the periodic/ alternating electric field is defined as follows:

$$a(t) = \frac{qE}{m} \cos(\omega t) \quad \text{Eq. 2-17}$$

$a(t)$ is then integrated after each collision (at $t = t_0$), under the initial conditions that require that the velocity is zero to obtain the speed, and a second integration to obtain $x(t)$. The boundary conditions require that $x(t)$ is continuous at $t = t_0$, to obtain $v(t)$ and $x(t)$ that are given by equations Eq. 2-18 and Eq. 2-19.

$$v(t) = \frac{qE}{\omega m} \sin(\omega t) - \frac{qE}{\omega m} \sin(\omega t_0), \quad v(t_0) = 0 \quad \text{Eq. 2-18}$$

$$x(t) = \frac{-qE}{\omega^2 m} \{\cos(\omega t) - \cos(\omega t_0)\} - \frac{qE}{\omega m} \{\sin(\omega t_0) (t - t_0)\} + x_0, \quad x(t_0) = x_0 \quad \text{Eq. 2-19}$$

Using Eq. 2-17 to Eq. 2-19, at any time t , the position, velocity, and acceleration of a charge carrier can be extracted. The model description indicates that a charge carrier must travel a certain distance, Δx , before a collision occurs. The probability ξ that the next collision happens at that distance, Δx , is given by

$$\xi = e^{-\frac{\Delta x}{\tau}} \quad \text{Eq. 2-20}$$

By using Eq. 2-20, a random number with an exponential distribution is generated using a uniform distribution or random numbers. This distance is sorted from this exponential distribution and thus given by Eq. 2-21.

$$\Delta x = -\lambda \log\{\text{rand}(0,1)\} \quad \text{Eq. 2-21}$$

Given a current position, the position for the next collision is obtained by selecting a random number between zero and one and multiplying the log of that number

by the mean free path (λ). Eq. 2-21 captures the fact that collisions occur at random due to imperfections in the material.

To find the time that said collision occurs, Eq. 2-19 is solved for Δt , thereby provides a time $t > t_0$ that a collision occurs at position $x = x_0 + \Delta x$. Following each collision, the initial condition, x_0 , or more generally x_i , is updated in Eq. 2-19 to reflect the new position at the collision point, and the process is now repeated. To illustrate this charge transport model, Table 2-1 summarizes the simulation input parameters, and Figure 2-2 shows the position, velocity, and acceleration of a charge over time. Given that t_0 shifts the initial conditions for the equation of motions, we will refer to it as time offset.

Table 2-1: *Simulation Input Parameters*

| Input Parameter | Value |
|------------------------|------------------------|
| E_0 | 10 N/C |
| λ | 4.3×10^{-9} m |
| Time Offset | 0 s |
| Frequency | 1.75×10^9 Hz |

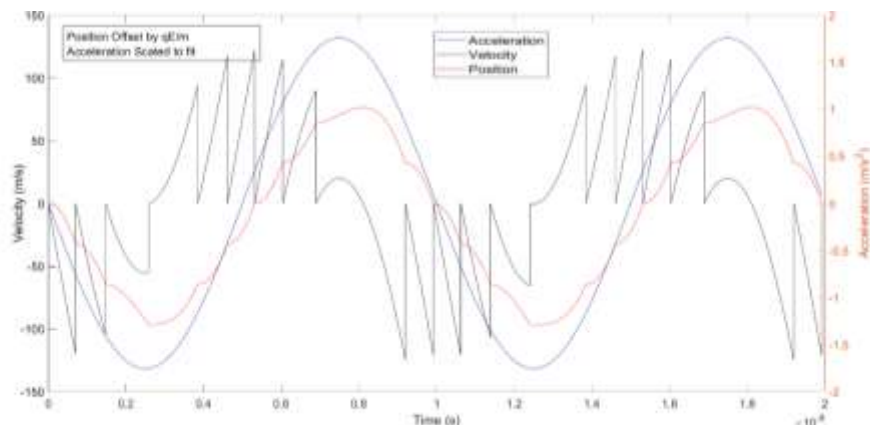


Figure 2-2: Charge carrier in a periodic electric field with multiple collisions.

The charge transport algorithm as implemented is shown in the flow diagram in Figure 2-3.

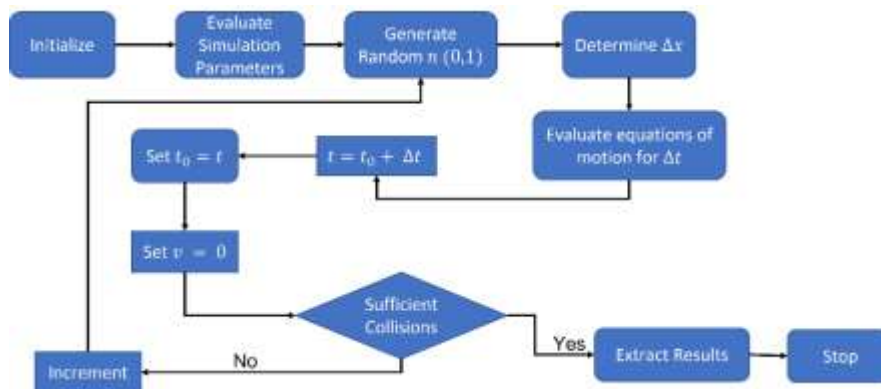


Figure 2-3: Charge transport model algorithm.

This transport model utilizes the mean free path, frequency, start time, and electric field as inputs to simulate transport of a charged particle through a material. The path of a single charge carrier is tracked, including details at all collision points. In order to address the challenge of the time complexity of this algorithm, collisions can be grouped into events. A single event represents a collection of n collisions. This event size can be any value; however, the following section uses an event size of $n = 5$. The

justification for this selection will be highlighted in Chapter 3. This process is broadly known as coarse graining.

2.3 Coarse Graining Methodology

Coarse graining aims to simulate the behavior of some complex event in a simplified manner. This is typically done at various granularity levels. This grouping allows for the transport characteristics previously highlighted, such as τ , to be generated from a probability distribution representing n collisions rather than explicitly evaluating every single collision based on a distance generated by Eq. 2-21 and inverting Eq. 2-19. Additionally, as illustrated in Table 2-1, multiple combinations of input parameters are possible. To perform exhaustive calculations at each combination of values would be both time-consuming and impractical. Coarse graining of the model, on the other hand, provides more efficient use of resources, provided that potential tradeoffs in accuracy are within acceptable limits. The details of the coarse graining process are outlined here.

Statistical analysis of characteristics such as time and distance traveled after n collisions were completed to coarse grain the model. One of the output parameters of interest, τ , as outlined in Eq. 2-14, was calculated and statistical analysis performed. To find the value for τ , collisions were grouped into events of $n=5$, and the time taken for the charge carrier to experience n collisions was recorded. To do this for individual collisions, the distance traveled is sorted from Eq. 2-21, and the flight time is obtained by inverting Eq. 2-19. This is repeated n times. τ is calculated as a simple average given by Eq. 2-22.

$$\tau_n = \frac{\sum_{i=1}^n t_i}{n} \quad \text{Eq. 2-22}$$

This computation was then repeated several times, and the results were compiled into a histogram. Analysis of the histogram's shape indicated that the data likely followed a combination of normal distributions. The probability density function for this distribution is outlined in Eq. 2-23.

$$f(t | \mu, \sigma, \zeta) = \sum_{i=1}^2 \zeta_i \cdot \frac{1}{\sigma_i \sqrt{2\pi}} e^{-\frac{1}{2} \left(\frac{t - \mu_i}{\sigma_i} \right)^2} \quad \text{Eq. 2-23}$$

Here, the mixing parameter $\zeta_2 = 1 - \zeta_1$ for $i=1, 2$. The parameters of the normal distribution presented above represent the mean (μ), standard deviation (σ), and mixing parameter (ζ). The mixing parameter (ζ) is essentially the probability that an observation will come from population i . The use of ζ easily allows for generating observations from a bimodal distribution with multiple μ and σ as in Eq. 2-23 above. Each unique set of input parameters provided slightly different outputs. Utilizing the parameters of this PDF, a distribution representing possible values of τ_n was generated. Now, instead of simulating each individual event, a random value can be sorted from the generated distribution and is equivalently treated as five collisions ($5\tau_n$). Since the possible variation in input parameters was essentially infinite, a limited number of start positions and electric fields were considered during the coarse graining process. That is to say that the possible start times within a cycle ($0 \leq t \leq \frac{2\pi}{\omega}$) can be broken down to a very fine level that is uncountably infinite. Therefore a limited number of start positions are selected within a cycle and explicitly used as the position at the start of a simulation. The homotopy is constructed by taking values of μ , σ and ζ and making them a function of the simulation parameters, in this case, start time, electric field, and frequency. Here the PDE parameters are first made a function of the start time and then a combination of start

time and electric field. Additionally, as this model considers periodic electric fields, the periodic nature of the model provides some additional simplification; the overall effects observed in the first half of a cycle were more or less duplicated in the second half of the cycle. As such, evaluating start times (Eq. 2-19) required only half of a cycle.

CHAPTER 3

HOMOTOPY ON START TIME

3.1 Homotopy Theory

A homotopy at base is a mapping of two continuous functions where one is morphed into the other. A topological space is a pair of objects (X, T) , where X is a non-empty set and T is a collection of subsets of X such that X and the null element are elements of T as well as the intersection and union of elements of T that are also elements of T . In appropriate notation:

1. $X \in T$
2. $\emptyset \in T$
3. If $O_1, O_2, \dots, O_n \in T$, then $O_1 \cap O_2 \cap \dots \cap O_n \in T$
4. If $\forall \alpha \in I, O_\alpha \in T$, then $\cup_{\alpha \in I} O_\alpha \in T$

Above, X is the underlying set, T is the topology on X , and all members of T are open sets [78].

Let $x, y \in X$, then X is said to be path-connected if there is a path that connects x to y for all x, y [78]. In a topological space, every path-connected space is generally connected. A space is connected if it cannot be partitioned into two open sets without breaking any path. Let X be a topological space that is path-connected; if X is disconnected, then $\exists A \neq \emptyset$ or $X \subset X \ni A$ that is both open and closed which is a contradiction.

Let $a \in A$ and $b \in C(A)$. Since X is path connected, $\exists f: [0,1] \rightarrow X \ni f(0) = a, f(1) = b$. $C(A)$ here represents the closure of A : all points in A and all limit points in A . Similarly, consider $B = \{t \ni f(t) \in A\}$. The set $B \neq \emptyset$ since $f(0) = a \in A$, and $B \neq [0,1]$ since $f(1) = b \notin A$. The set B is, therefore, either open or closed but not both since $[0,1]$ is connected, and A can similarly be open or closed but not both [78].

Let f_1, f_2 be paths in X that connect x to y where $x, y \in X$, then f_1 is said to be homotopic to f_2 if $\exists H: [0,1]^2 \rightarrow X$, where H is continuous and the following hold true for $0 \leq x, t \leq 1$.

$$H(0, t) = x$$

$$H(1, t) = y$$

$$H(s, 0) = f_1(s)$$

$$H(s, 1) = f_2(s)$$

The function H here is called the homotopy connecting f_1 to f_2 and both belong to the same homotopy class. In a simply connected space, any path between two points can be deformed into any other space [78]. A homotopy can be viewed as a set of paths within the space of continuous functions H , connecting two points in the space such that one can be deformed into the other. An alternative view of a homotopy is one of a family of continuous paths from f_1 to f_2 . For every point $s \in I$, there is a path from $f_1(s)$ to $f_2(s)$ [78], therefore as long as a path exists, the two are connected.

3.2 Preliminaries to a Homotopy on Start Time

The coarse graining of the model is presented in this section. Due to how this model is built, the position of a carrier is determined by the time. This is illustrated in Eq. 2-17 to Eq. 2-19. Since position can be determined from time, it is not strictly necessary

to track the position of the carrier, as the equivalent evaluation of start time provides similar information. Additionally, different start times are implemented via a time offset, that is, some $t \geq 0$ which indicates the start of the simulation.

Before evaluating the overall effects of the start time on average collision time and conductivity, a preliminary study was done to determine how changes in start time affected end time after five collisions (1 event). By start time, we mean the part of the cycle where the charge is first observed. The idea was to simulate charge transport after a single event, then repeat the process a set number of times and evaluate the results. Results from the baseline model are discussed below. A sample size of $m=10,000$ events was used as a baseline for the final evaluation. The choice of $m=10,000$ event is based on a comparative study described in Figure 3-1.

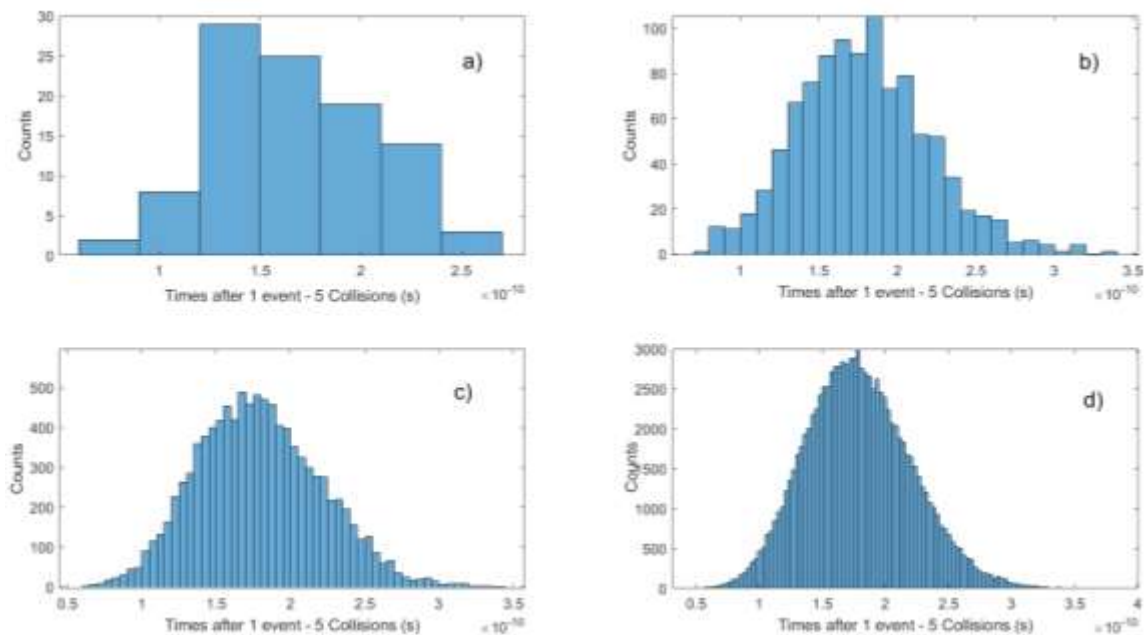


Figure 3-1: Comparison of distributions with varying total number of events (m) describing time data a) 100 events b) 1,000 events c) 10,000 events d) 100,000 events.

Each order of magnitude, starting at 100 until 100,000, was evaluated with simulation input parameters outlined in Table 3-1. In each case, the only difference was the total number of events. The parameter used for these simulations are reported in Table 3-2. The procedure can be summarized as follows. A particular time within a cycle is chosen as starting time, and the position for the next collision is determined randomly based on the mean free path. The flight time is calculated from Eq. 2-21. From the place and time of the last collision, the displacement until the next collision is randomly chosen, and the time calculated from Eq. 2-21. This process is repeated for a total of n collisions, and the collision time is averaged for the n collisions. This n -collision event is what is referred to as an event in this document. The process is repeated for a chosen number of events m . This average flight time is assumed to be distributed according to normal distribution or a bimodal distribution consisting of two Gaussian distributions. A histogram of event flight time is used to parameterize the normal distributions.

Table 3-1: *Simulation Input Parameters*

| Input Parameter | Value |
|------------------------|------------------------|
| E_0 | 30 N/C |
| λ | 4.3×10^{-9} m |
| Time Offset | 0 s |
| Frequency | 1×10^7 Hz |
| Carrier Density | 8.491×10^{28} |

Table 3-2: PDF Parameters for Estimates for Different Numbers of Events

| Number of events | μ (s) | σ (s) | ζ |
|------------------|-------------------------|-------------------------|---------|
| 100 | 1.668×10^{-10} | 4.019×10^{-11} | 1.0 |
| 1,000 | 1.813×10^{-10} | 4.172×10^{-11} | 1.0 |
| 10,000 | 1.790×10^{-10} | 4.185×10^{-11} | 1.0 |
| 100,000 | 1.791×10^{-10} | 4.183×10^{-11} | 1.0 |

The results presented in Figure 3-1 and Table 3-2 indicate that a selection of 1000 events or greater may be appropriate for parameter estimation. The difference between 1,000 and 10,000 is less than 1%. Above 10,000 events, there is minimal change in the values of μ and σ . The difference is less than 0.1% between 10,000 and 100,000. To further test the quality of the probability distributions, collision times were sorted from these distributions with parameters provided in Table 3-2 to those from the original histogram (Figure 3-1). The results of this comparison are presented in Figure 3-2.

A visual inspection of Figure 3-2 indicated that a) where 1,000 events were simulated was the least similar to the original histogram, while d) was the most similar. To quantify the comparison, a similarity score was defined and used.

The similarity score S between A and B , with $0 \leq S(A, B) \leq 1$, from less similar to more similar, is expressed by Eq. 3-1, where A_i and B_i are the bin height in the normalized histogram A and B , respectively.

$$S(A, B) = 1 - \sum_i |A_i - B_i| \quad \text{Eq. 3-1}$$

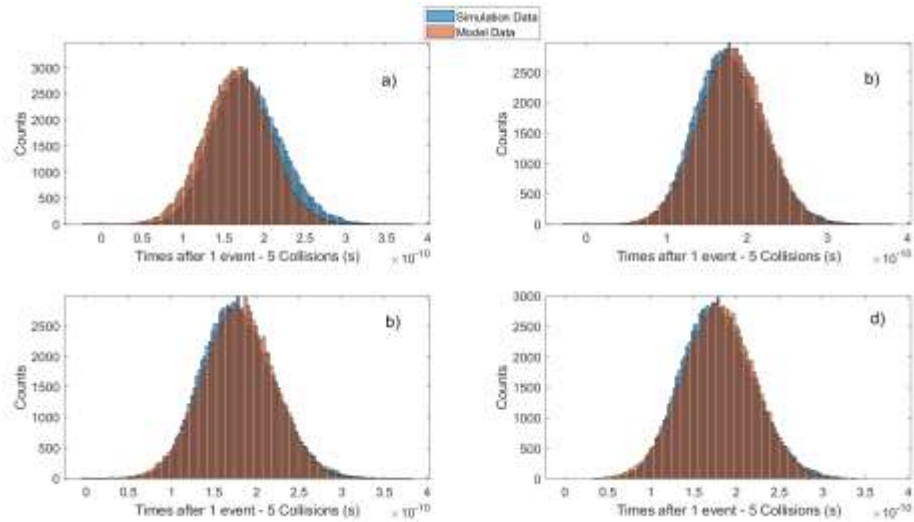


Figure 3-2: Comparison of distributions with varying total number of events (n) describing time data a) 100 events b) 1,000 events c) 10,000 events d) 100,000 events with original simulation data overlaid.

If $S(A, B) = 0$, there is no overlap between A and B. A score larger than zero indicates some similarity; the two histograms have some bins that overlap, and the larger the score, the larger the overlap. The closer to 1, the larger the similarity. The similarity of a histogram to itself, $S(A, A)$ is equal to 1. It is important to note that the number and size of the bins are the same in both histograms. The larger the absolute difference in heights of the bins, the lower the similarity. Since bin locations are fixed, a quantitative measurement can be achieved and compared as needed.

The results are reported in Table 3-3.

Table 3-3: Similarity of Histogram Data for Time to 1 Event

| Event Size (m) | Similarity |
|-----------------------|-------------------|
| 100 | 80.260% |
| 1,000 | 89.312% |
| 10,000 | 92.090% |
| 100,000 | 92.104% |

The results in Table 3-3 show a moderate improvement in similarity as the total number of events increases. The similarity for 100,000 events is only 0.014% higher than for 10,000 events which is already above 90%. This indicates that it is not cost-effective to go above 10,000 events. Conversely, there is a clear difference in similarity between 100 events and 1,000 events. With a difference of over 9%, the benefits outweigh the costs in this instance. The difference in similarity from 1,000 to 10,000 events, less than 3%, may be small enough for some applications, so simulating between 1,000 and 10,000 events is at the user's discretion. However, overall, the similarity between the average collision time generated from a coarse-grained simulation and one where each collision is simulated individually is below 90%, which was considered the lowest acceptable benchmark based on previous tests. These previous smaller scale simulations indicated that with similarity values of under 85%, the error in values generated from distributions was relatively high (over 20%). At a similarity of 90% or above, these same tests indicate that the error was less than 10%, in some cases, less than 1%; therefore, a benchmark of 90% was set. While the tradeoff in simulation time is significant, the increase in accuracy at 10,000 events meets the accuracy benchmark. The above indicates that it is possible to

coarse-grain the charge transport model by groupings of collisions without significantly reducing accuracy.

Another area of interest was in the total simulation time of the coarse-grained model versus the individual simulations. A comparison of the total simulation time was conducted for the sample sizes in Figure 3-3. An important provision must be made here. Despite these individual simulations being run on the QB2 cluster, task parallelism was not implemented since each charge carrier is independent of the other. Rather, data parallelism was implemented, with up to 20 different data streams being processed simultaneously. The times reported here are equivalent to a single data stream being processed by a single processor. The times used in Figure 3-3 represent the shortest times lapsed for a single run at each event level.

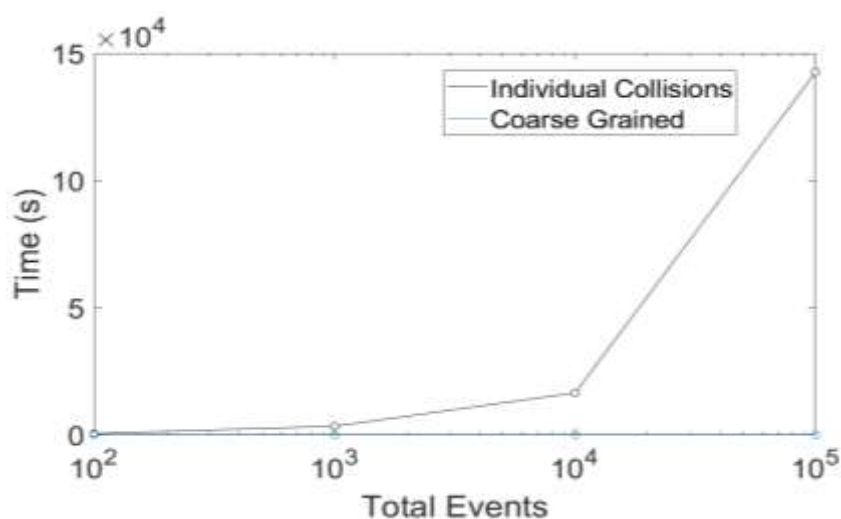


Figure 3-3: Comparison of individual collision simulation time and coarse-grained times for generation of various numbers of events (m).

The data presented in Figure 3-3 indicate a minimum speedup in wall time of at least 800 times the original simulation time. On the larger scale of total events, a speedup of over 11,000 times the original simulation time was observed. The most

time-consuming component of the transport routine is eliminated by sorting from a distribution and thus the speed up. Indeed, a significant part of the speedup is observed from sorting random numbers from a probability distribution in the coarse-grained model rather than having to solve equations for each collision. Similarly, if probability distributions were created for every collision instead of every five collisions, a very significant speedup would still be achieved. The speed up due to the coarse graining will roughly scale with n . The raw values are shown in Table 3-4.

Table 3-4: *Simulation Time for Individual Collisions and a Coarse-Grained Model*

| Events | Individual Collisions (s) | Coarse Grained (s) |
|---------------|----------------------------------|---------------------------|
| 100 | 438 | 0.5 |
| 1,000 | 3321 | 1.5 |
| 10,000 | 16416 | 2.5 |
| 100,000 | 142560 | 12 |

While there is a slight tradeoff in accuracy, the significant time savings make this model a good option, provided that approximately 92% accuracy is reasonable. Higher accuracy is possible; however, the tradeoff in computation time is significantly larger than in the preceding case; therefore, a baseline of 10,000 events was selected as the optimal option for the model and its associated developments.

3.3 Homotopy on Start Time

3.3.1 Grain Size of $n=5$

While section 3.2 outlined the results of the coarse-graining process, this was merely the first step, confirming that coarse-graining was possible. This section deals with the results of developing the homotopy on start time. As previously mentioned, the

position of a charge carrier can be determined if the time that carrier is in said position is known. However, the distribution of travel time will depend on the initial position in the cycle or the starting point of the carrier. In other words, if the initial time is such that the field is at a maximum, then the travel time between collisions will be shorter since acceleration is larger than if, at the starting time, the electric field magnitude is small. To evaluate this, multiple simulations were conducted with eight initial starting times, each corresponding to a specific start position within a single cycle. These points are shown in Table 3-5.

Table 3-5: *Summary of Simulation Start Times and Corresponding Positions (+ and - Indicate the Direction of Movement)*

| Offset Name | Position Offset (m) | Time Offset (s) |
|-------------|-------------------------|-----------------------|
| B | 1.34×10^{-3} | 0 |
| B/2 + | 6.68×10^{-4} | 1.67×10^{-8} |
| 0 + | 2.17×10^{-19} | 2.5×10^{-8} |
| -B/2 + | -6.68×10^{-4} | 3.33×10^{-8} |
| -B | -1.34×10^{-3} | 5.0×10^{-8} |
| -B/2 - | -6.68×10^{-4} | 6.67×10^{-8} |
| 0 - | -2.17×10^{-19} | 7.5×10^{-8} |
| B/2 - | 6.68×10^{-4} | 8.33×10^{-8} |

Note that due to the symmetry of the problem, starting at B is the same as starting at -B, as there is a mirror symmetry around the origin. The only difference is the signs of the time offset indicating the direction of movement. This was further explored, and Figure 3-4 shows the minimum and maximum time for one event based on 10,000 total events per time offset from Table 3-5. This shows some semblance of symmetry when

considering all simulations for different start times and the minimum and maximum values are approximated repeated at each half cycle.

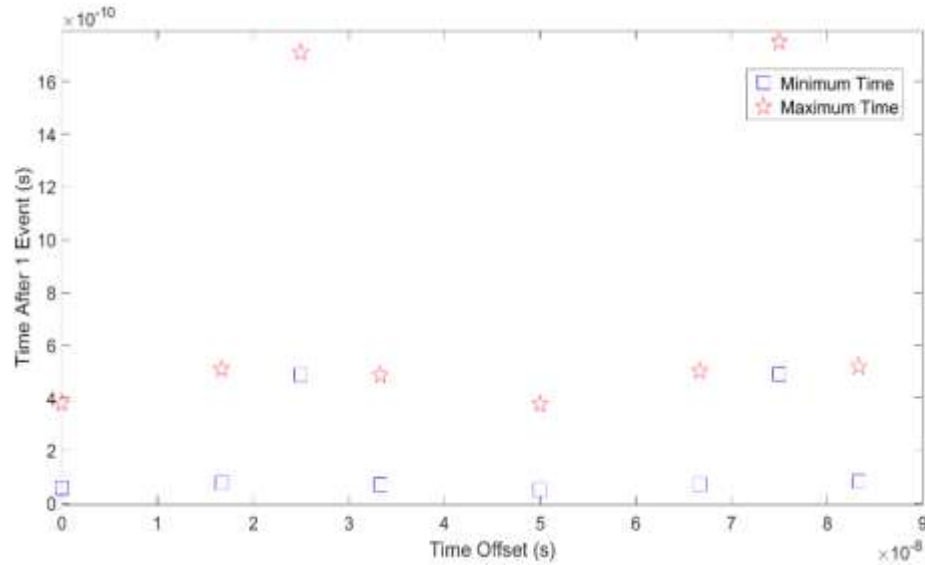


Figure 3-4: Comparison of select start times and eventual stopping times after one event.

Due to the rather large differences in the intervals of the selected start times, the granularity needed to be decreased. The intent was to evaluate any trends in the data and their utility for building the homotopy on start time. Additionally, instead of looking at the minimum and maximum times, the mean and standard deviation were investigated. The simulation input parameters for Figure 3-4 and Figure 3-5 were the same as those shown in Table 3-1.

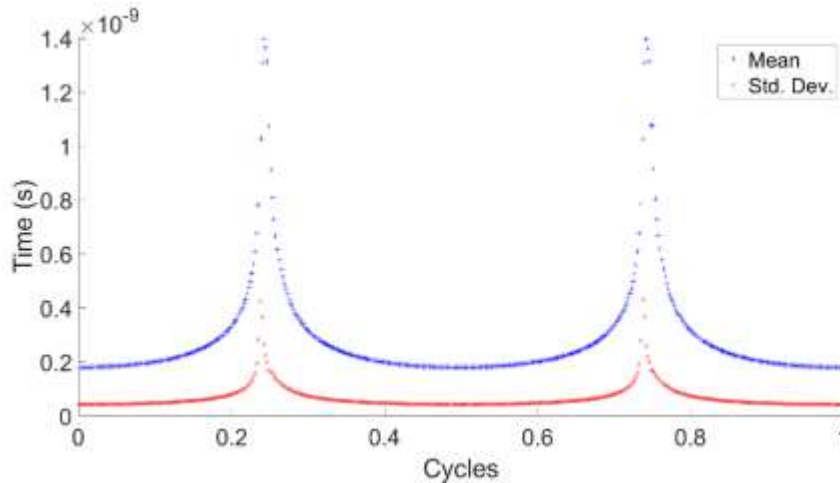


Figure 3-5: Comparison of select start times and parameters describing distributions of total flight time after one event.

Figure 3-5 represents a more granular investigation of how start time affected the mean and standard deviation of the datasets. Four hundred eighty intermediate points were selected within a single cycle based on the Frequency (from 0 to $1/F$). For each start time, 10,000 events were generated similar to the results presented in 3.2 and analyzed likewise by calculating μ and σ . The results shown in Figure 3-5 also confirmed, to a greater extent, the symmetry of the problem observed in the previous section: the average carrier flight time relative to its starting time is symmetric. This implies that the problem can be reduced to a $1/2$ cycle.

By using the information from Figure 3-5, a homotopy on start time was created, where given any start time t from a continuum between B and $-B$, the distribution of flight times for one event (5 collisions) can be constructed from the homotopy between PDFs with parameters that are a continuous function of the start time. The function defining the parameters is fit by using the parameters determined for start time specifically simulated. In other words, μ_i and σ_i , the parameters of a normal distribution that better fit the

histogram of average collision times for specific start times t_i are used to fit continuous functions $\mu(t_i)$ and $\sigma(t_i)$ that span a certain interval of starting times. The homotopy $H(t_i)$ is then:

$$H(t_i | \mu, \sigma) = \frac{1}{\sigma(t_i)\sqrt{2\pi}} e^{-\frac{1}{2}\left(\frac{t-\mu(t_i)}{\sigma_i}\right)^2} \quad \text{Eq. 3-2}$$

With Eq. 3-2, the flight time for an event consisting of n collisions can be sorted out for any start time in the first half of cycle s $t_i = \left[\frac{2(s-1)\pi}{\omega}, \frac{(2s-1)\pi}{\omega}\right]$ For instance, $s = 0$ is the first cycle Eq. 3.2 can be evaluated for any value in $t_i = \left[0, \frac{\pi}{\omega}\right]$. The second half of the interval $t_0 = \left[\frac{(1s-1)\pi}{\omega}, \frac{2s\pi}{\omega}\right]$ being mirror symmetric to the first half; therefore, for a start time in that second have, Eq. 3-2 is evaluated at a symmetric mirror time in the first half.

Initial results from the homotopy were relatively mixed. When the individual collision simulation data were compared to the coarse-grained data from the homotopy, start times near the center of the interval (1/4 cycle) produced relatively poor results: the highest similarity score was less than 50%. These required some additional investigation. A visual inspection of the data within this range shows that at those starting times, the distribution is actually bimodal and cannot be represented by a single Gaussian distribution. Figure 3-6 shows an example of this issue, while Table 3-6 outlines the specific simulation input parameters for that run.

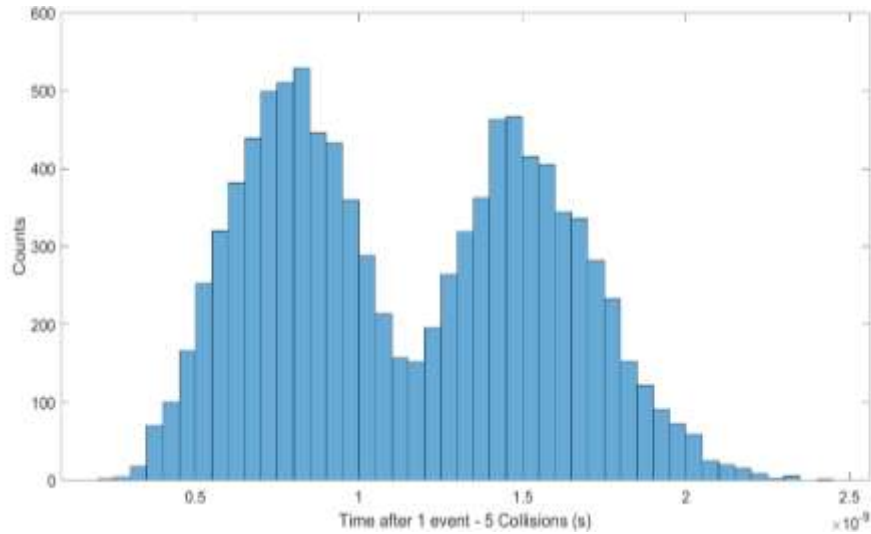


Figure 3-6: Histogram of data with time offset near $\frac{1}{4}$ of a cycle

Table 3-6: *Simulation Input Parameters*

| Parameter | Value |
|-------------|--------------------------|
| E_0 | 30 N/C |
| λ | 4.3×10^{-9} m |
| Time Offset | 2.403×10^{-8} s |
| Frequency | 1×10^7 Hz |

With the simulation input parameters outlined above, the bimodality was observed with a time offset between 2.3673×10^{-8} s and 2.4285×10^{-8} s. While this interval is relatively small, the goal of this work is to create a homotopy (mapping) that can provide an end time given any start time within a $\frac{1}{2}$ cycle. If only one event were considered, this would not be too significant. However, the homotopy should be able to predict the end time of continuous events. That is, for two events E_i and E_{i+1} , the starting point of E_{i+1} is calculated by adding the sorted flight time to the starting time of E_i . If the

paths from E_i to E_{i+1} are not convergent, then the mapping is inaccurate and thus not applicable. However, if there are convergent paths (f_j) that connect E_i and E_{i+1} , then these paths are homotopic to each other.

Further analysis of the data around the region of interest (between 2.3673×10^{-8} s and 2.4285×10^{-8} s) revealed that the bimodality was both gradual and predictable. This was noted when an additional 50 start times within and near that region were investigated. By utilizing a combination of two Gaussians with a mixing parameter (ζ) that determines the relative contribution of each of the two normal distributions (Eq. 2-22), a proper homotopy at these troubled time intervals was built. Overall, the homotopy for the half cycle is presented as a seven-part piecewise function, with the coefficient of determination ranging from $0.8077 \leq R^2 \leq 0.9950$ in both μ and σ . Each section of the piecewise function was fit to a polynomial of degree 2:

$$(t) = P_1 t^2 + P_2 t + P_3 \quad \text{Eq. 3-2}$$

The standard deviation, mean, and mixing parameter are all represented by the form of Eq. 3-2. Additionally, as illustrated in Figure 3-6, to handle the bimodality, a combination of normal distributions was used in one particular interval. These areas are shown in Table 3-7 with μ_2 , σ_2 and ζ being the representations of these binomials for the interval $2.3622 \times 10^{-8} < t \leq 2.4336 \times 10^{-8}$. Table 3-7 summarizes the fit parameters and intervals, delimited by the lower and upper bound, where they apply.

Table 3-7: Homotopy on Start Time Parameters

| | P_1 | P_2 | P_3 | Lower (s) | Upper(s) |
|-------------------|--------------------------|--------------------------|--------------------------|-------------------------|-------------------------|
| $f_{\mu_1}(t)$ | 7.687×10^{-12} | 1.919×10^{-11} | 1.916×10^{-10} | 0 | 1.6250×10^{-8} |
| | 2.008×10^{-11} | 6.487×10^{-11} | 3.114×10^{-10} | 1.6250×10^{-8} | 2.2500×10^{-8} |
| | 1.440×10^{-11} | 6.925×10^{-11} | 5.533×10^{-10} | 2.2500×10^{-8} | 2.3622×10^{-8} |
| | -5.203×10^{-11} | -2.987×10^{-11} | 7.781×10^{-10} | 2.3622×10^{-8} | 2.4336×10^{-8} |
| | 3.591×10^{-11} | -3.102×10^{-10} | 1.086×10^{-9} | 2.4336×10^{-8} | 2.6250×10^{-8} |
| | 2.917×10^{-11} | -8.328×10^{-11} | 3.334×10^{-10} | 2.6250×10^{-8} | 3.2500×10^{-8} |
| | 9.439×10^{-12} | -2.204×10^{-11} | 1.922×10^{-10} | 3.2500×10^{-8} | 5.0000×10^{-8} |
| $f_{\sigma_1}(t)$ | 1.890×10^{-12} | 4.562×10^{-12} | 4.480×10^{-11} | 0 | 1.6250×10^{-8} |
| | 5.705×10^{-12} | 1.647×10^{-11} | 7.346×10^{-11} | 1.6250×10^{-8} | 2.2500×10^{-8} |
| | 9.406×10^{-12} | 2.574×10^{-11} | 1.394×10^{-10} | 2.2500×10^{-8} | 2.3622×10^{-8} |
| | -4.816×10^{-21} | -7.574×10^{-21} | 3.506×10^{-20} | 2.3622×10^{-8} | 2.4336×10^{-8} |
| | 1.425×10^{-11} | -5.167×10^{-11} | 1.772×10^{-10} | 2.4336×10^{-8} | 2.6250×10^{-8} |
| | 5.324×10^{-12} | -1.723×10^{-11} | 7.702×10^{-11} | 2.6250×10^{-8} | 3.2500×10^{-8} |
| | 2.133×10^{-12} | -5.014×10^{-12} | 4.489×10^{-11} | 3.2500×10^{-8} | 5.0000×10^{-8} |
| $f_{\zeta_1}(t)$ | 6.121×10^{-2} | -5.841×10^{-2} | 4.337×10^{-1} | 2.3622×10^{-8} | 2.4336×10^{-8} |
| $f_{\mu_2}(t)$ | 6.523×10^{-11} | -1.193×10^{-10} | -7.777×10^{-11} | 2.3622×10^{-8} | 2.4336×10^{-8} |
| $f_{\sigma_2}(t)$ | 2.696×10^{-20} | -4.046×10^{-20} | 6.931×10^{-20} | 2.3622×10^{-8} | 2.4336×10^{-8} |

The second mixing parameter $f_{\zeta_2}(t)$ is found as simply as the complement of $f_{\zeta_1}(t)$, $f_{\zeta_2}(t) = 1 - f_{\zeta_1}(t)$ as it is the probability of the complementary event occurring. When used in concert, the functions presented in Table 3-7 represent the homotopy on start time, whereby the time of flight of a carrier can be predicted with a grain size of $n = 5$. Further, since the entire space is path connected, that is, there exists a path from any point within the space to another, events can be chained together. For a series of

connected events, E , the end point of event E_i becomes the start point of event E_{i+1} . A comparison homotopy-based coarse-grained simulation with simulations where collisions are individually accounted for results is presented in Figure 3-7 to Figure 3-11 and Table 3-8 and Table 3-9.

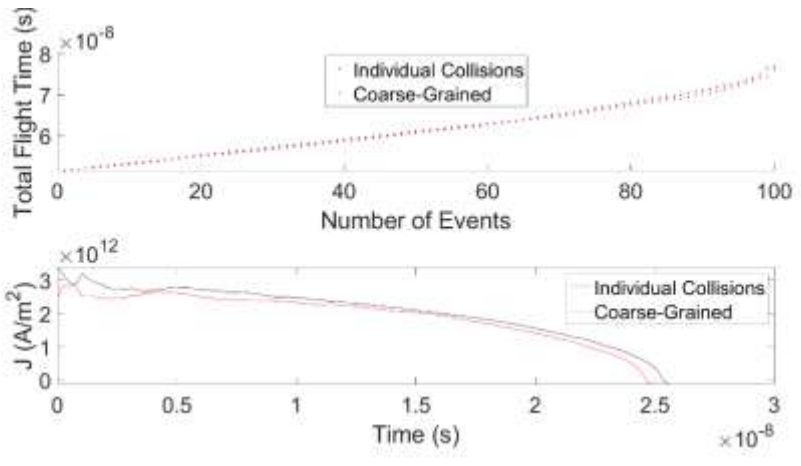


Figure 3-7: Homotopy on start time for 100 events showing total flight time a) and Current Density b).

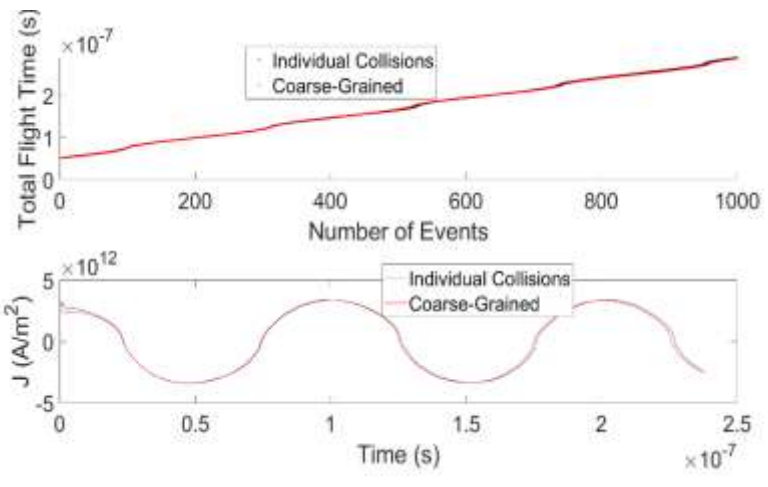


Figure 3-8: Homotopy on start time for 1,000 events showing total flight time a) and Current Density b).

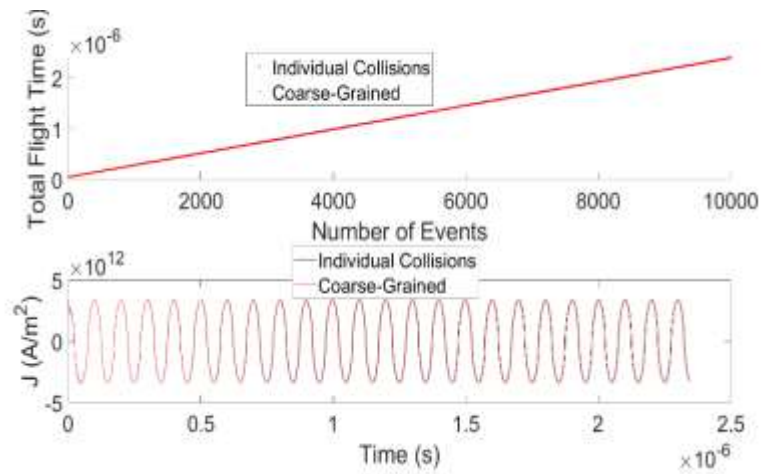


Figure 3-9: Homotopy on start time for 10,000 events showing total flight time a) and Current Density b).

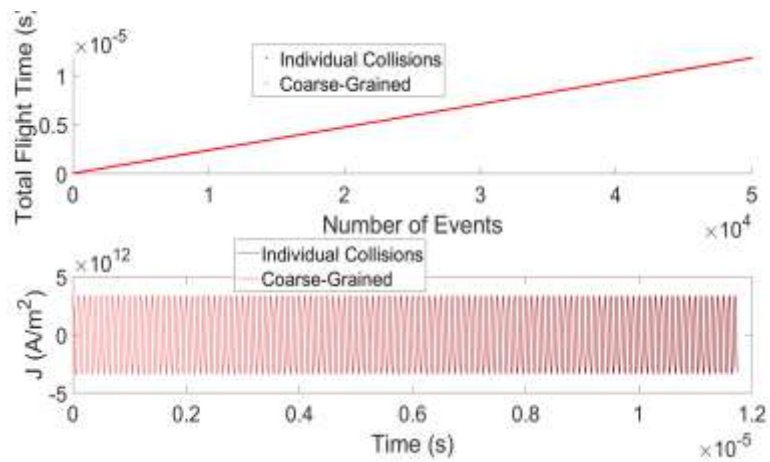


Figure 3-10: Homotopy on start time for 50,000 events showing total flight time a) and current density b).

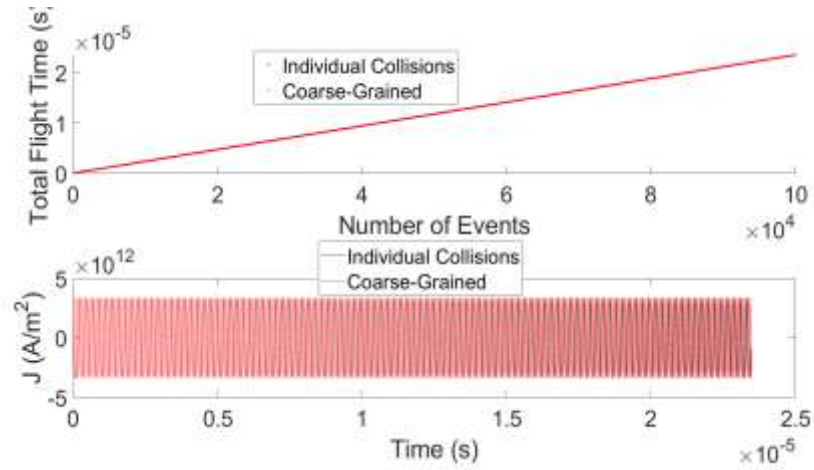


Figure 3-11: Homotopy on start time for 100,000 events showing total flight time a) and Current Density b).

Table 3-8: *Individual Collisions (IC) and Coarse-Grained (CG) Model Average Collision Time (τ) for Select Total Events*

| # Event | τ_{IC} (s) | τ_{CG} (s) | % Difference |
|---------|-------------------------|-------------------------|--------------|
| 100 | 5.124×10^{-11} | 4.981×10^{-11} | 2.81% |
| 1,000 | 4.765×10^{-11} | 4.738×10^{-11} | 0.56% |
| 10,000 | 4.692×10^{-11} | 4.684×10^{-11} | 0.17% |
| 50,000 | 4.698×10^{-11} | 4.695×10^{-11} | 0.07% |
| 100,000 | 4.694×10^{-11} | 4.696×10^{-11} | 0.04% |

Table 3-9: *Individual Collisions (IC) and Coarse-Grained (CG) Model Peak Current Density (J_{rms}) for Select Total Events*

| # Event | $J_{rms_{IC}} (A/m^2)$ | $J_{rms_{CG}} (A/m^2)$ | % Difference |
|----------------|------------------------|------------------------|--------------|
| 100 | 2.601×10^{12} | 2.528×10^{12} | 2.81% |
| 1,000 | 2.418×10^{12} | 2.405×10^{12} | 0.56% |
| 10,000 | 2.382×10^{12} | 2.378×10^{12} | 0.17% |
| 50,000 | 2.385×10^{12} | 2.383×10^{12} | 0.07% |
| 100,000 | 2.383×10^{12} | 2.384×10^{12} | 0.04% |

From Table 3-8 and Table 3-9, as well as the preceding figures (Figure 3-7 to Figure 3-11), it is evident that utilizing the presented homotopy to model charge transport in a coarse-grained manner can provide significant benefits. Primary among them is the reduction in computational complexity compared to tracking individual carriers. On the other hand, since the model is based on Monte Carlo methods, low numbers of events, as illustrated in Figure 3-7, may not appropriately represent the phenomenon. For 100 events, a percentage difference of 2.81% is observed. However, for a larger number of events, the model quickly increases in accuracy, as shown for $m \geq 1,000$ events. This lower accuracy for smaller values of m is not a significant issue, as charge carriers will typically collide thousands of times in a fraction of a second. One of the limitations of the model, as presented in this section, is that it is only applicable to a single electric field and a single frequency at a time. An expansion will be provided in Chapter 4. Before getting into that, notice that in this section, only a grain size of $n=5$ has been considered. The following section evaluates the same concept but for a different grain size of $n=50$.

3.3.2 Grain Size of $n=50$

By utilizing the gained foreknowledge as reported in the previous section, additional analysis was completed to assess how a different grain size might affect the accuracy of the homotopy on start time. Similar simulations were completed, except only 120 unique start times were evaluated along a $\frac{1}{2}$ cycle. Results from Figure 3-5 confirmed the symmetry and the decision to lower the number of points based on the intervals from previous results. For each unique start time, $m=10,000$ events were simulated, where a single event is $n=50$ collisions. Each set of events was analyzed separately, and a normal distribution was fit to the data. Unlike the case of $n=5$, no start times where the resultant data were bimodal were found. The mean and standard deviation for all start times is shown in Figure 3-12.

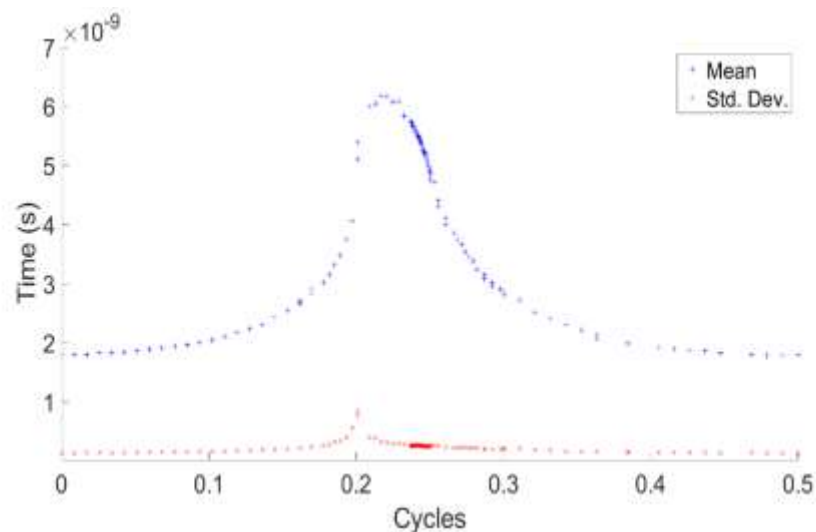


Figure 3-12: Comparison of select start times and parameters describing distributions of total flight time after $n=50$ collisions (1 event).

There is a clear trend in the parameters, as it was found for the smaller grain size of $n=5$. The simulation input parameters were the same as those previously presented in

Table 3-1. One observation of note was that between $0 \leq t \leq 1.75 \times 10^{-8}$ in Figure 3-12, the mean and standard deviation was approximately 10 times those of Figure 3-5. The same is true for $3 \times 10^{-8} \leq t \leq 5 \times 10^{-8}$. Since the total number of collisions representing an event is 10 times more than for $n=5$. This is expected because the carrier will travel 10 times longer than in the case of $n=5$; thus, the mean will increase proportionally. A mapping was then built, and thus the homotopy on start time was created. The homotopy is presented as a piecewise function of 3 parts, with the coefficient of determination $R^2 \geq 0.9432$ in both mu and sigma. Each section of the piecewise function is a quadratic function (Eq. 3-3) or a 2-term exponential function (Eq. 3-4). The second and third parts of the piecewise functions for μ and σ respectively are quadratic, while the other parts are 2-term exponentials. Table 3-10 summarizes the fit parameters and intervals along which they apply.

$$f(t) = P_1 t^2 + P_2 t + P_3 \quad \text{Eq. 3-3}$$

$$f(t) = P_1 e^{P_2 t} + P_3 e^{P_4 t} \quad \text{Eq. 3-4}$$

Table 3-10: Homotopy on Start Time Coefficients

| | P_1 | P_2 | P_3 | P_4 |
|---------------|--------------------------|--------------------------|-------------------------|-------------------------|
| $f_\mu(t)$ | 1.920×10^{-9} | 4.310×10^{-2} | 2.045×10^{-10} | 1.838 |
| | -2.389×10^{-10} | 7.432×10^{-11} | 6.179×10^{-9} | - |
| | 1.639×10^{-9} | -1.291 | 1.600×10^{-9} | 1.224×10^{-2} |
| $f_\sigma(t)$ | 1.440×10^{-10} | 7.986×10^{-2} | 1.302×10^{-11} | 2.661 |
| | 3.408×10^{-11} | -1.618 | 2.807×10^{-10} | -6.810×10^{-5} |
| | 1.302×10^{-11} | -6.314×10^{-11} | 2.067×10^{-10} | - |

The parameters in Table 3-10 apply along three time intervals: $0 \leq t_1 < 2.102 \times 10^{-8}$, $2.102 \times 10^{-8} \leq t_2 < 2.328 \times 10^{-8}$ and $2.328 \times 10^{-8} \leq t_3 < 5.0 \times 10^{-8}$. When used in concert, the functions presented in Table 3-10 represent the homotopy on start time, whereby the time of flight of a carrier can be predicted with a grain size of $n = 50$. Since the space is path connected, events can be chained. A comparison of the results of the homotopy compared to individual simulation results is presented in Figure 3-13 to Figure 3-17 and Table 3-11.

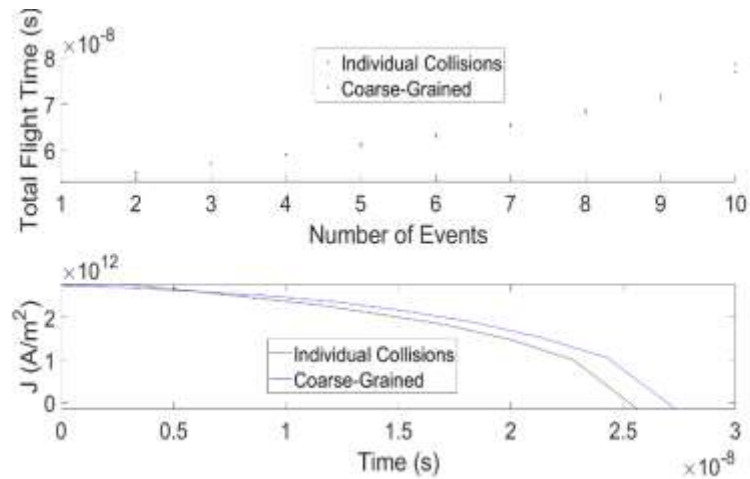


Figure 3-13: Homotopy on start time for 10 events showing total flight time a) and Current Density b).

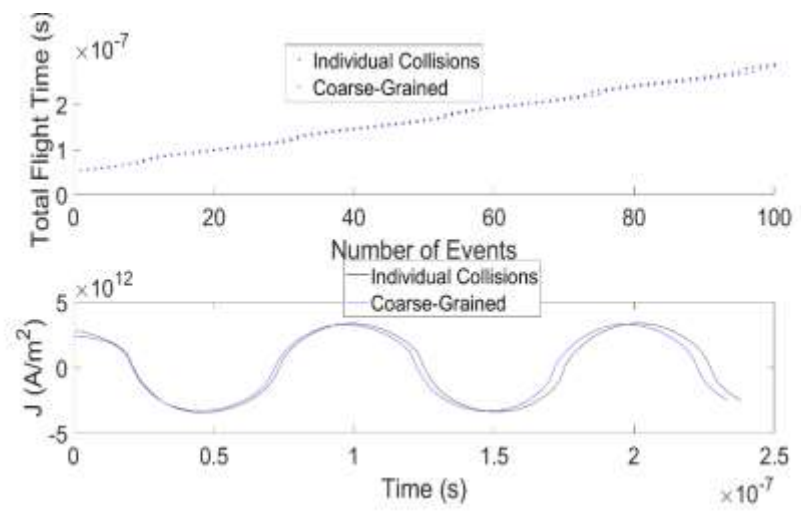


Figure 3-14: Homotopy on start time for 100 events showing total flight time a) and Current Density b).

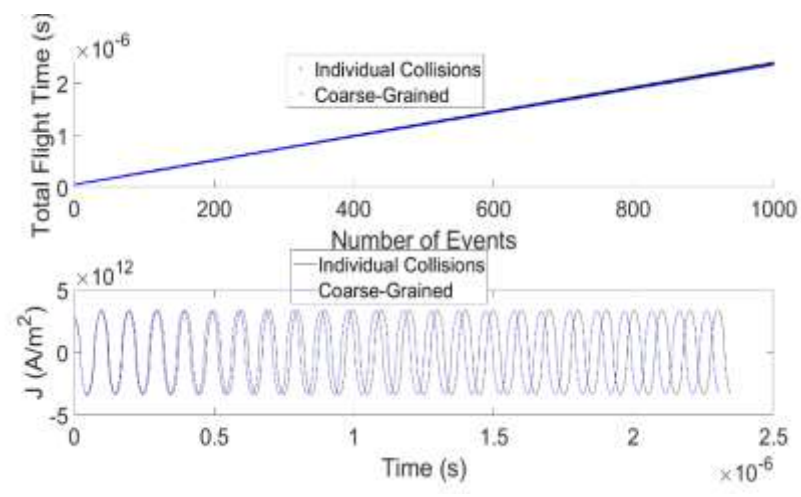


Figure 3-15: Homotopy on start time for 1,000 events showing total flight time a) and Current Density b).

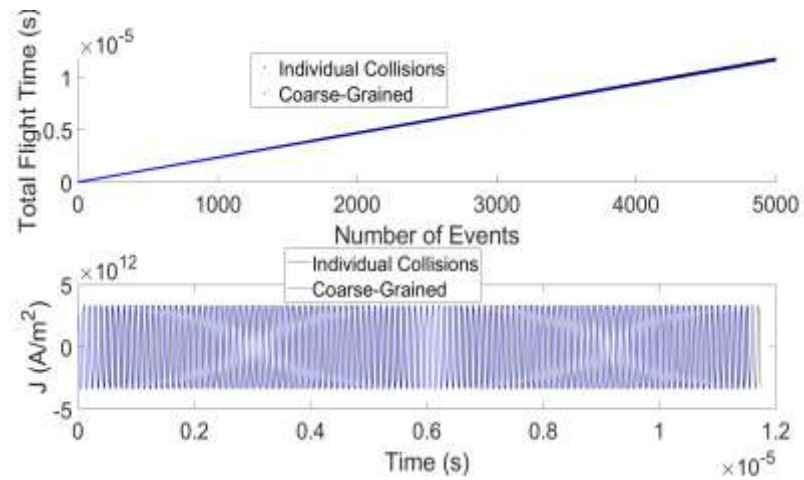


Figure 3-16: Homotopy on start time for 5,000 events showing total flight time a) and Current Density b).

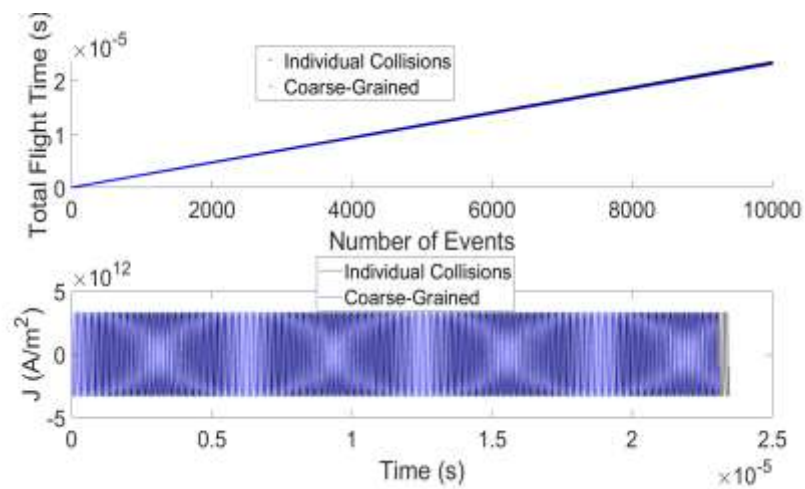


Figure 3-17: Homotopy on start time for 10,000 events showing total flight time a) and Current Density b).

Table 3-11: *Individual Collisions (IC) and Coarse-Grained (CG) Model Average Collision Time (τ) for Select Total Events*

| # Event | τ_{IC} (s) | τ_{CG} (s) | % Difference |
|----------------|-------------------------|-------------------------|--------------|
| 100 | 5.124×10^{-11} | 5.467×10^{-11} | 6.7% |
| 1,000 | 4.765×10^{-11} | 4.666×10^{-11} | 2.1% |
| 10,000 | 4.692×10^{-11} | 4.611×10^{-11} | 1.7% |
| 50,000 | 4.698×10^{-11} | 4.622×10^{-11} | 1.6% |
| 100,000 | 4.694×10^{-11} | 4.620×10^{-11} | 1.6% |

The results presented in Figure 3-13 to Figure 3-17 indicate that while the homotopy is valid, it is not as accurate with a grain size of 50. This is particularly clear in Figure 3-17, where 10,000 events are modeled and compared to the original simulation data, where each collision is explicitly tracked. Clearly, there is some difference as the carrier proceeds in time. This is again evident in Table 3-12, which shows a percentage error between 6.7% and 1.6% over different numbers of events. There may be multiple reasons for this divergence; however, the most likely is that due to the larger number of collisions grained together, some macro phenomena captured at a smaller grain size may be missed and the effect accumulated over time. However, although 1.6% is large compared to the error when $n=5$, it is not a large difference in itself for most applications. The type of fine details that are evidenced in a smaller grouping of collisions, such as the clear bimodality illustrated in Figure 3-6, are not as readily evident with larger grain sizes. Of significance, however, the current density values calculated with this size grain are relatively near the true values, typically a difference of at least 1.6% and at most 6.7%. Despite this, the clear difference seen for large numbers of events forces a more

careful choice of the number of events to model. Nevertheless, the homotopy parameters provided an R^2 values consistently over 94.32% for all parts.

Table 3-12: *Individual Collisions (IC) and Coarse-Grained (CG) Model Current Density (J_{rms}) for Select Total Events*

| # Event | $J_{rms_{IC}} (A/m^2)$ | $J_{rms_{CG}} (A/m^2)$ | % Difference |
|---------|------------------------|------------------------|--------------|
| 100 | 2.601×10^{12} | 2.775×10^{12} | 6.7% |
| 1,000 | 2.418×10^{12} | 2.369×10^{12} | 2.1% |
| 10,000 | 2.382×10^{12} | 2.340×10^{12} | 1.7% |
| 50,000 | 2.385×10^{12} | 2.350×10^{12} | 1.6% |
| 100,000 | 2.383×10^{12} | 2.345×10^{12} | 1.6% |

3.3.3 Effect of Grain Size on Current Density

Figure 3-18 explores how the total flight time changes with different grain sizes and compares them to the case of individual collision simulations. In order to perform this comparison, the largest grain size was used as the standard, and others were granulated to achieve the same number of collisions. While a single event in the case of $n=5$ represented five collisions grouped together, to achieve the same level of granularity with the larger grain size of $n=50$, 10 events where one event is five collisions were simulated successively with the end time of the previous event becoming the start time of the next, and the result at the end extracted. Similarly, in the case where each individual collision is tracked (essentially a grain size of $n=1$), events are grouped together to achieve the required granularity level of $n=50$ for comparison.

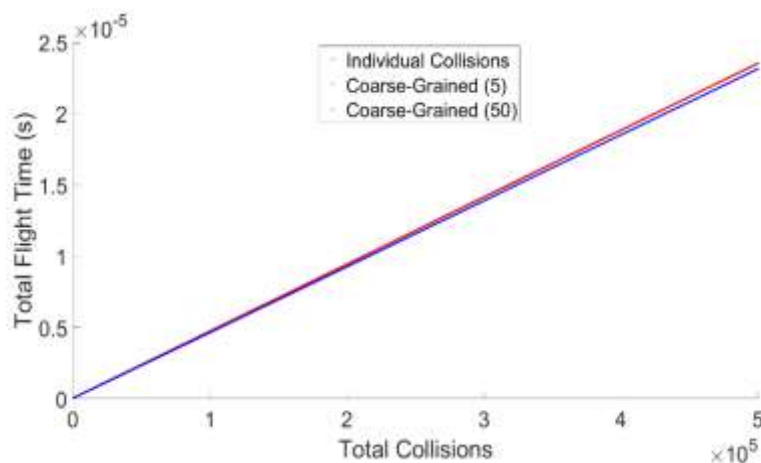


Figure 3-18: Comparison of total flight time of source simulation against homotopy with $n=5$ and $n=50$

Figure 3-18 shows the comparison of the homotopies in start time for different grain sizes with the results where individual collisions are tracked. The homotopy constructed with a grain size of $n=50$ seems to diverge slightly as the number of events increases. In the case of $n=5$, the total flight time is very similar to that of the source simulation. It can be inferred from Figure 3-18 that a grain size of $n=5$ is more representative of the coarse-grained charge transport process than at $n=50$. Since both the average collision time and the peak current density depend on the total flight time, it is a similar divergence will be observed in these results. The current density is presented in Figure 3-19 and Table 3-13 and Table 3-14.

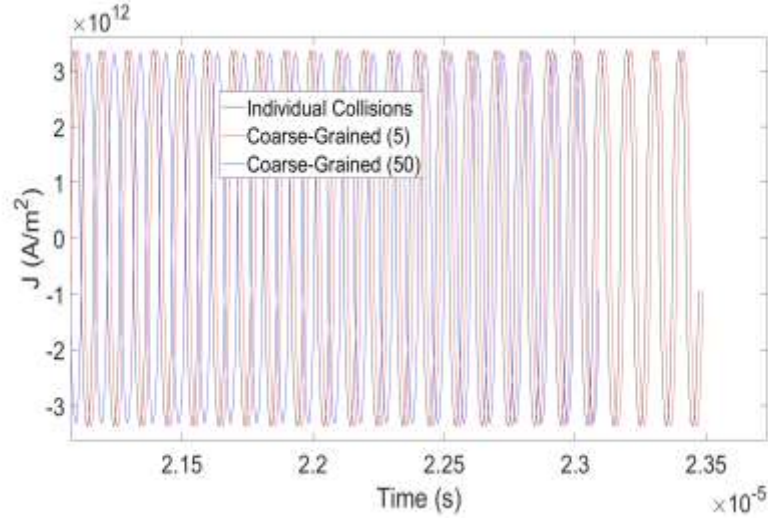


Figure 3-19: Current density compared across individual collisions, and homotopy of $n=5$ and $n=50$.

Table 3-13: Individual collisions (IC) and coarse-grained (CG) models current density (J_{rms}) for 500,000 collisions

| # Collisions | $J_{rms_{IC}}$ (A/m^2) | $J_{rms_{CG_5}}$ (A/m^2) | $J_{rms_{CG_{50}}}$ (A/m^2) |
|--------------|----------------------------|------------------------------|---------------------------------|
| 500,000 | 2.383×10^{12} | 2.390×10^{12} | 2.345×10^{12} |

Table 3-14: Individual collisions (IC) and coarse-grained (CG) model average collision time (τ) for 500,000 collisions

| # Collisions | τ_{IC} (s) | τ_{CG} (s) | $\tau_{CG_{50}}$ (s) |
|--------------|-------------------------|-------------------------|-------------------------|
| 500,000 | 4.694×10^{-11} | 4.708×10^{-11} | 4.619×10^{-11} |

As with the total carrier flight time, a finer representation of the tails of the plot is available in below. It is observed from the figures above that the homotopy on start time with a grain size of $n=50$ is not as good a representation of the original simulation data. Rather, with a grain size of $n=5$, the homotopy appears to predict the individual collision simulation values more closely.

This holds true for all three of the output values presented above: total carrier flight time, average collision time, and current density. Additionally, the percentage difference between the source simulation values and both homotopies were analyzed for different total events. It was observed that the percentage error decreases faster as the total number of events increases for $n=5$ than for $n=50$. Since both $n=5$ and $n=50$ provide similar results with minimal effect on accuracy at higher numbers of events, a grain size of $n=5$ was chosen for the next step in the parametrical homotopy as the final option since they are near equivalent. However, it is acknowledged that the efficiency of this approach increases with the size of the grain. Figure 3-20 shows the comparison of the total flight time of the source simulation against homotopy.

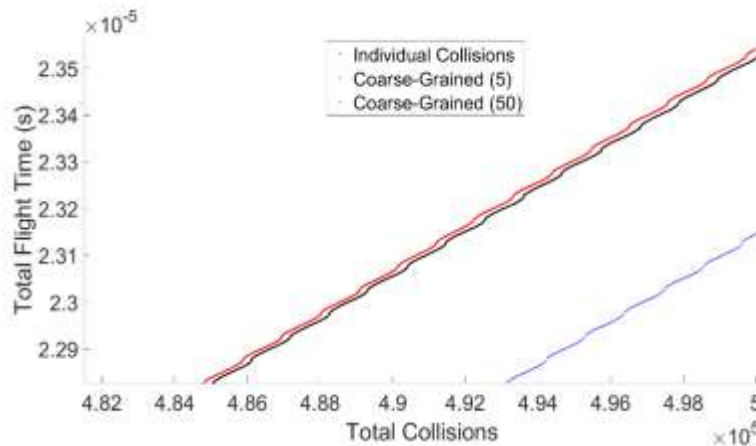


Figure 3-20: Comparison of total flight time of source simulation against homotopy with $n=5$ and $n=50$ – Finer View

Despite the accuracy of the presented model, it is only useful for a single electric field and frequency. In an effort to improve the model and make it more widely usable, a two-dimensional homotopy is discussed in Chapter 4.

CHAPTER 4

HOMOTOPY ON START TIME AND ELECTRIC FIELD

4.1 Homotopy in Two Dimensions

The coarse-grained model presented in Chapter 3 utilized a homotopy on start time to predict the total flight time of a charge carrier after $n=5$ collisions (1 event). This model, while useful, is limited in scope since it only varies a single input variable, the start time. An attempt was made to increase the usability of this model by extending it to another input variable, namely electric field.

As outlined in the introduction and Chapter 2 of this dissertation, a charge carrier under the effects of a periodic electric field in an ohmic conductor will suffer collisions. These collisions alter the path of the carrier. Depending on the variation in the peak electric field, the maximum distance that a carrier can travel within a single period changes. Additionally, this can influence the conductance and current density of the material. As a result, the effects of different peak electric fields must be determined and accounted for in this homotopy.

4.1.1 Evaluation of Effects of the Electric Field

The transport characteristics of the charge carrier depend on the electric field. In order to quantify this effect, the carrier motion was simulated for a range of 14 electric fields were chosen between 10 N/C and 100 N/C, and the distributions for 280 different start times (for each field) within a half cycle were calculated and compared. A grain size

of $n=5$ collisions was chosen for convenience. For each unique electric field, 10,000 events were simulated per start time: after five collisions had occurred, the start time was reset and repeated 10,000 times. Other input parameters included $\lambda = 4.3 \times 10^{-9}$ and frequency of 1×10^7 Hz. The value used for the carrier density was 8.491×10^{28} . The data on each of these runs were collected, analyzed, and presented in Figure 4-1.

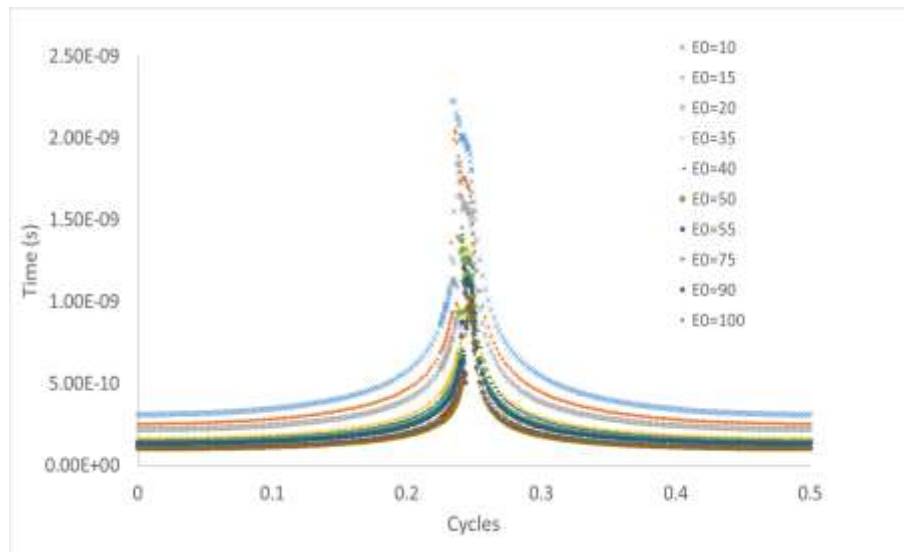


Figure 4-1: Parameter estimates for mean (μ) across electric fields and start times.

The standard deviation across the different electric fields follows a similar trend as the mean shown above. Note that in Figure 4-1, as the amplitude of the electric field increases, the mean values decrease, and the peak becomes thinner (see). This is also outlined in Table 4-1.

Table 4-1: Comparison of Average Collision Time (τ) for Various Electric Field Amplitudes after 1 Event

| # Collisions | Time offset = 0 (s) | ¼ Cycle (s) | ½ Cycle (s) |
|--------------|------------------------|------------------------|------------------------|
| $E_0 = 10$ | 3.09×10^{-10} | 1.56×10^{-9} | 3.10×10^{-10} |
| $E_0 = 15$ | 2.53×10^{-10} | 1.36×10^{-9} | 2.53×10^{-10} |
| $E_0 = 20$ | 2.19×10^{-10} | 1.23×10^{-9} | 2.19×10^{-10} |
| $E_0 = 35$ | 1.66×10^{-10} | 1.02×10^{-9} | 1.66×10^{-10} |
| $E_0 = 40$ | 1.54×10^{-10} | 9.79×10^{-10} | 1.55×10^{-10} |
| $E_0 = 50$ | 1.38×10^{-10} | 9.09×10^{-10} | 1.38×10^{-10} |
| $E_0 = 55$ | 1.32×10^{-10} | 8.80×10^{-10} | 1.32×10^{-10} |
| $E_0 = 75$ | 1.14×10^{-10} | 7.92×10^{-10} | 1.13×10^{-10} |
| $E_0 = 90$ | 1.03×10^{-10} | 7.46×10^{-10} | 1.03×10^{-10} |
| $E_0 = 100$ | 9.82×10^{-11} | 7.22×10^{-10} | 9.83×10^{-11} |

This behavior implies that the carrier flight time for an event is less likely to be found around these higher mean values: as the electric field increases, the probability of a charge carrier's total flight time being at or near a ¼ cycle decreases; hence the thin peaks. The decreased probability is because of the carrier spending less time within said regions and being less likely to need more than five times the average collision time during the total flight. In addition to these observations, each electric field contained a subset of start times where the data was bimodal; they required a combination of multiple Gaussians to properly represent the data, similar to the case presented in Figure 3-6. This subset of start times was located before the ¼ cycle point for all electric fields evaluated. In the case of a single electric field, the start times in question would be a single interval. With multiple electric fields being considered, some consideration had to be given on

how best to account for this bimodality throughout these areas across the different electric fields.

The start times that resulted in the bimodal data were collected and compared for each dataset. A path, represented by a function on the electric fields, was then constructed that would predict the point at which this bimodality begins and ends. This gave the benefit of reducing the overall complexity of the model. The functions that predicted the start ($L(E)$) and end ($U(E)$) points of bimodality as a function of the electric field are presented in equations 4-1 and 4-2.

$$L(E_0) = 3.924297e^{-10} \log(E_0) + 2.23231e^{-8}, \quad 10 \leq E_0 \leq 100 \quad \text{Eq. 4-1}$$

$$U(E_0) = 1.39198e^{-10} \log(E_0) + 2.37309e^{-8}, \quad 10 \leq E_0 \leq 100 \quad \text{Eq. 4-2}$$

Using Eq. 4-1 and Eq. 4-2, the lower ($L(E)$) and upper ($U(E)$) start times, where a combination of two gaussians is required to describe the data, can be predicted. These functions are necessary to predict the region of bimodality for electric fields that have not been explicitly included in the parametrization of the model. Eq. 4-1 and Eq. 4-2 will provide the start and end points of this bimodality. These functions are valid for the expressed electric field range, from 10 to 100 N/C. Following the construction of this mapping function, an attempt to develop a two-dimensional homotopy in start time and electric field was made.

4.1.2 2-D Homotopy Construction

In order to incorporate the second dimension into the homotopy, the model required some modifications. Since the version of the homotopy outlined in 3.3.1 for a single dimension was well developed, similar simulations were required to implement the second dimension. The same process was repeated for 14 electric fields, with only nine of

them being used to build the homotopy and the rest to test it. In other words, combinations of the nine cases were used to determine the parameters of the homotopical function that then were evaluated to correspond to one of the other five, so they could be compared. Data for one electric field ($E_0 = 10N/C$) were eliminated entirely due to inconsistencies in the dataset: repeated simulations gave widely different parameter estimates. With no obvious reason for the differences despite some investigation, therefore the lower limit was moved to 15 N/C. The idea here was to perform a split on the data by using 64% of the data to parameterize the homotopy and the other 36% to test the parametrization. This was a basic split test. The rationale for using this methodology was because the process of determining the parameters is relatively time-consuming (based on the 1-D model), as a lot of data was available to construct the model. In cases where model construction is expensive (large dataset and time-consuming processes), the basic split test is one of the most used methods, [79] in addition to providing test cases for the parametrization.

Another option for building the homotopy and separating the data into testing and training sets is k-fold cross validation. In k-fold cross validation, data is partitioned into k equally sized segments or folds, and k iterations of training and validation are performed [80]. Within each iteration, a different fold of data is held out for validation while the remaining k-1 folds are used for parametrization. In the end, all the accuracy predictions are averaged, and an overall performance measure is obtained. While a k-fold cross validation method may have possibly provided more accuracy overall and improved performance, this method is not ideal when handling large datasets. With large datasets,

sampling of each fold is recommended or performing a split test. As a result, the split test was used.

To create the mapping, parameters representing the 280 start positions and nine electric fields were generated and analyzed. For each unique electric field, a piecewise function of seven parts was used, representing the homotopy for that particular field. Each of these parts was represented as polynomials of degree 2. The parameters for each part were then fit to a function of the electric field. The result of this was a function of two variables, t and E_0 , which was then used to generate coefficients representing the parameters for μ and σ . A representation of this is outlined below for the two types of results (polynomial and logarithmic functions). Each parameter (P_1 , P_2 , or P_3) is generated either by a 2nd degree polynomial (Eq. 4-3) or a logarithmic function (Eq. 4-4). The selection of one or the other is based on the number of coefficients that apply to that particular parameter. If there are three coefficients, then the form of Eq. 4-3 applies. If there are two coefficients, then the form of Eq. 4-4 applies.

$$P_{i_{\mu/\sigma/\zeta}}(E_0) = (\alpha_{\mu} E_0^2 + \beta_{\mu} E_0 + \gamma_{\mu}) \quad \text{Eq. 4-3}$$

$$P_{i_{\mu/\sigma/\zeta}}(E_0) = (\alpha_{\mu} \ln E_0 + \beta_{\mu}) \quad \text{Eq. 4-4}$$

A function similar to Eq. 4-3 or Eq. 4-4 represents a single coefficient for a particular section of the piecewise function. Once these coefficients (P_1 , P_2 and P_3) have been determined, they are then used to create a function of the form shown below, which is identical to Eq. 3-2.

$$f(t, E_0) = P_1(E_0)t^2 + P_2(E_0)t + P_3(E_0) \quad \text{Eq. 4-5}$$

To properly represent the entire interval, 51 coefficients needed to be represented across the different electric fields leading to a total of 17 functions comprising the two-

dimensional homotopy. These 17 functions are all polynomials of the form of Eq. 4-5 and are for 7-part piecewise functions for μ_1 and σ_1 . μ_2 , σ_2 and ζ also follow the same form, but are a single function each. Table 4-2 outlines the simulation input parameters used to generate the data used to construct the homotopy. Table 4-3 to Table 4-5 shows the coefficients of these functions and the parameters they represent.

Table 4-2: *Simulation Input Parameters for 2-D Homotopy*

| Input Parameter | Value |
|-----------------|---|
| E_0 | [15, 20, 35, 40, 50, 55, 75, 90, 100] N/C |
| λ | 4.3×10^{-9} m |
| Time Offset | 0 - 5×10^{-8} s |
| Frequency | 1×10^7 Hz |

Table 4-3: *Two-Dimensional Homotopy Coefficients for μ_2 , σ_2 and ζ between $L(E_0) \leq t \leq U(E_0)$*

| | Param. | α | β | γ |
|------------------------|--------|--------------------------|--------------------------|--------------------------|
| $f_{\mu_2}(E_0, t)$ | P_1 | -4.592×10^{-2} | 8.800×10^{-2} | - |
| | P_2 | -2.995×10^{-5} | 3.853×10^{-3} | -3.605×10^{-1} |
| | P_3 | 9.542×10^{-2} | 3.727×10^{-1} | - |
| $f_{\sigma_2}(E_0, t)$ | P_1 | 1.664×10^{-14} | -2.135×10^{-12} | -6.690×10^{-11} |
| | P_2 | -3.816×10^{-14} | 4.433×10^{-12} | -4.289×10^{-11} |
| | P_3 | -4.515×10^{-10} | 3.145×10^{-9} | - |
| $f_{\zeta}(E_0, t)$ | P_1 | 2.625×10^{-19} | 7.020×10^{-1} | - |
| | P_2 | 2.554×10^{-20} | -1.360×10^{-19} | - |
| | P_3 | -3.663×10^{-20} | 2.016×10^{-19} | - |

Table 4-4: *Two-Dimensional Homotopy Coefficients for μ*

| | Param. | α | β | γ | L Lim | U Lim |
|-------------------------------------|--------|--------------------------|--------------------------|--------------------------|-------------------------|-------------------------|
| $f_{u_1}(\mathbf{E}_0, \mathbf{t})$ | P_1 | -3.377×10^{-12} | 1.915×10^{-11} | - | 0 | 1.6250×10^{-8} |
| | P_2 | -8.584×10^{-12} | 4.865×10^{-11} | - | | |
| | P_3 | -8.630×10^{-11} | 4.926×10^{-10} | - | | |
| $f_{u_2}(\mathbf{E}_0, \mathbf{t})$ | P_1 | -7.218×10^{-12} | 3.957×10^{-11} | - | 1.6250×10^{-8} | 2.2500×10^{-8} |
| | P_2 | -2.493×10^{-11} | 1.393×10^{-10} | - | | |
| | P_3 | -1.366×10^{-10} | 7.771×10^{-10} | - | | |
| $f_{u_3}(\mathbf{E}_0, \mathbf{t})$ | P_1 | 1.739×10^{-12} | 9.223×10^{-12} | - | 2.2500×10^{-8} | 2.3622×10^{-8} |
| | P_2 | -1.061×10^{-11} | 1.133×10^{-10} | - | | |
| | P_3 | -2.298×10^{-10} | 1.341×10^{-9} | - | | |
| $f_{u_4}(\mathbf{E}_0, \mathbf{t})$ | P_1 | 1.332×10^{-11} | 8.341×10^{-11} | - | 2.3622×10^{-8} | 2.4336×10^{-8} |
| | P_2 | -1.371×10^{-14} | 1.788×10^{-12} | -4.564×10^{-11} | | |
| | P_3 | -2.375×10^{-10} | 1.602×10^{-9} | - | | |
| $f_{u_5}(\mathbf{E}_0, \mathbf{t})$ | P_1 | -2.760×10^{-15} | 3.224×10^{-13} | -6.881×10^{-12} | 2.4336×10^{-8} | 2.6250×10^{-8} |
| | P_2 | 7.082×10^{-16} | 1.203×10^{-13} | -4.037×10^{-11} | | |
| | P_3 | -6.718×10^{-11} | 4.512×10^{-10} | - | | |
| $f_{u_6}(\mathbf{E}_0, \mathbf{t})$ | P_1 | -2.095×10^{-11} | 1.755×10^{-10} | - | 2.6250×10^{-8} | 3.2500×10^{-8} |
| | P_2 | 6.447×10^{-11} | -4.337×10^{-10} | - | | |
| | P_3 | -2.035×10^{-10} | 1.161×10^{-9} | - | | |
| $f_{u_7}(\mathbf{E}_0, \mathbf{t})$ | P_1 | -7.899×10^{-12} | 4.537×10^{-11} | - | 3.2500×10^{-8} | 5.0000×10^{-8} |
| | P_2 | 1.625×10^{-11} | -9.329×10^{-11} | - | | |
| | P_3 | -8.885×10^{-11} | 5.077×10^{-10} | - | | |

Table 4-5: Two-Dimensional Homotopy Coefficients for σ_1

| | Param. | α | β | γ | L Lim | U Lim |
|--|--------|--------------------------|--------------------------|--------------------------|-------------------------|-------------------------|
| $f_{\sigma_1}(\mathbf{E}_0, \mathbf{t})$ | P_1 | -3.377×10^{-12} | 1.915×10^{-11} | - | 0 | 1.6250×10^{-8} |
| | P_2 | -8.584×10^{-12} | 4.865×10^{-11} | - | | |
| | P_3 | -8.630×10^{-11} | 4.926×10^{-10} | - | | |
| $f_{\sigma_2}(\mathbf{E}_0, \mathbf{t})$ | P_1 | -7.218×10^{-12} | 3.957×10^{-11} | - | 1.6250×10^{-8} | 2.2500×10^{-8} |
| | P_2 | -2.493×10^{-11} | 1.393×10^{-10} | - | | |
| | P_3 | -1.366×10^{-10} | 7.771×10^{-10} | - | | |
| $f_{\sigma_3}(\mathbf{E}_0, \mathbf{t})$ | P_1 | 1.739×10^{-12} | 9.223×10^{-12} | - | 2.2500×10^{-8} | 2.3622×10^{-8} |
| | P_2 | -1.061×10^{-11} | 1.133×10^{-10} | - | | |
| | P_3 | -2.298×10^{-10} | 1.341×10^{-9} | - | | |
| $f_{\sigma_4}(\mathbf{E}_0, \mathbf{t})$ | P_1 | 1.332×10^{-11} | 8.341×10^{-11} | - | 2.3622×10^{-8} | 2.4336×10^{-8} |
| | P_2 | -1.371×10^{-14} | 1.788×10^{-12} | -4.564×10^{-11} | | |
| | P_3 | -2.375×10^{-10} | 1.602×10^{-9} | - | | |
| $f_{\sigma_5}(\mathbf{E}_0, \mathbf{t})$ | P_1 | -2.760×10^{-15} | 3.224×10^{-13} | -6.88×10^{-12} | 2.4336×10^{-8} | 2.6250×10^{-8} |
| | P_2 | 7.082×10^{-16} | 1.203×10^{-13} | -4.037×10^{-11} | | |
| | P_3 | -6.718×10^{-11} | 4.512×10^{-10} | - | | |
| $f_{\sigma_6}(\mathbf{E}_0, \mathbf{t})$ | P_1 | -2.095×10^{-11} | 1.755×10^{-10} | - | 2.6250×10^{-8} | 3.2500×10^{-8} |
| | P_2 | 6.447×10^{-11} | -4.337×10^{-10} | - | | |
| | P_3 | -2.035×10^{-10} | 1.161×10^{-9} | - | | |
| $f_{\sigma_7}(\mathbf{E}_0, \mathbf{t})$ | P_1 | -7.899×10^{-12} | 4.537×10^{-11} | - | 3.2500×10^{-8} | 5.0000×10^{-8} |
| | P_2 | 1.625×10^{-11} | -9.329×10^{-11} | - | | |
| | P_3 | -8.885×10^{-11} | 5.077×10^{-10} | - | | |

Tables 4-3 to Table 4-5 provide the coefficients representing the homotopy in start time and electric field. In cases where only two coefficients are provided (α & β), the function representing the mapping takes the form of Eq. 4-4. In the cases where there are three coefficients, the function representing the mapping takes the form of Eq. 4-3.

These coefficients are combined to represent 17 unique functions that represent the full homotopy. Each coefficient was calculated via a curve fit on the coefficients. The different fits for these parameters were relatively good, with 36 of 51 of them having an $R^2 \geq 0.80$. Nine of the 51 parameters had an $0.5 \geq R^2 < 0.80$ were considered marginally acceptable. The remaining six parameters were considered a bad fit with sub 0.5 R^2 values. These marginal and bad fits could potentially adversely affect the model, however, due to the nature Monte Carlo, the errors could offset each other, something that will be confirmed during the validation stage.

Within this half cycle and electric fields from 15 to 100 N/C, any combination of start time and electric field can easily be coarse-grained by evaluating $\mu(t, E_0)$, $\sigma(t, E_0)$, and $\zeta(t, E_0)$. Since a path exists connecting all these functions in the space, they are connected and belong to the same homotopy class. To test the homotopy, the transit time, and current density for an applied field $E_0 = 55 \text{ N/C}$ was calculated from a simulation where each individual collision was considered and compared with those obtained from the homotopy function. The electric field of $E_0 = 55 \text{ N/C}$ was one of those included in the data split. Results are shown in Figure 4-2 to Figure 4-4 for $m=500$ and Figure 4-5 to Figure 4-7 for $m=20,000$ events and Table 4-6 and Table 4-7. Error bars in Figure 4-2 are calculated as the root mean squared error.

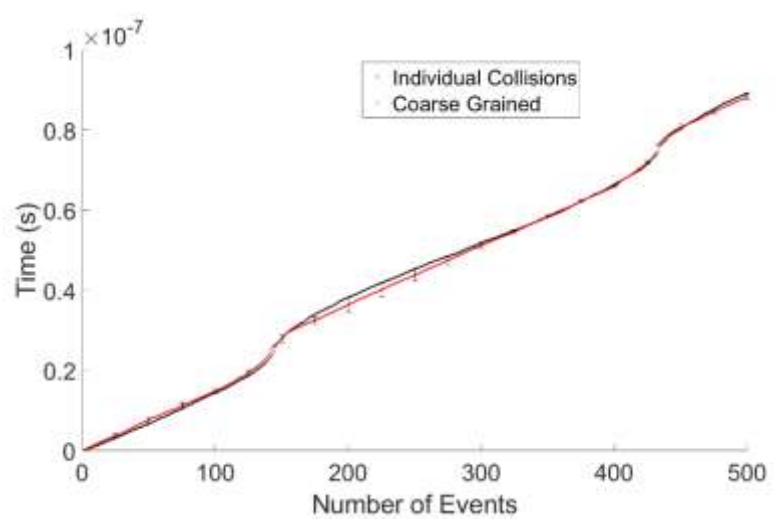


Figure 4-2: Total flight time of individual Collisions against Coarse Grained Model on electric fields and start times with $m=500$ events, $E=55$ N/C.

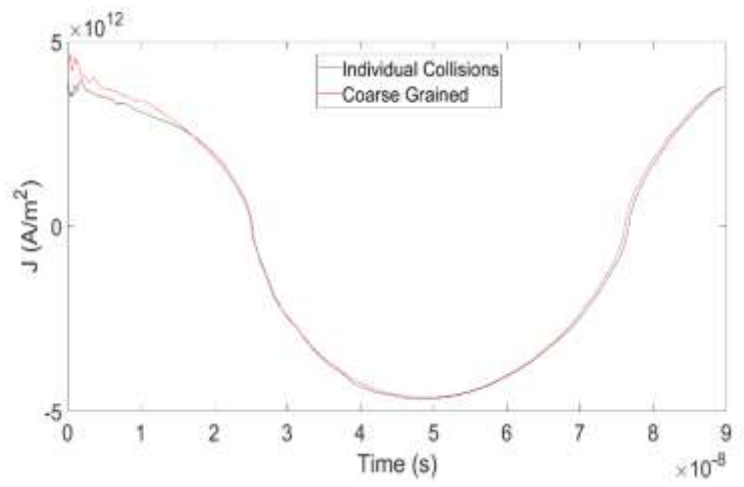


Figure 4-3: Current Density of individual Collisions against Coarse Grained Model on electric fields and start times with $m=500$ events, $E=55$ N/C.

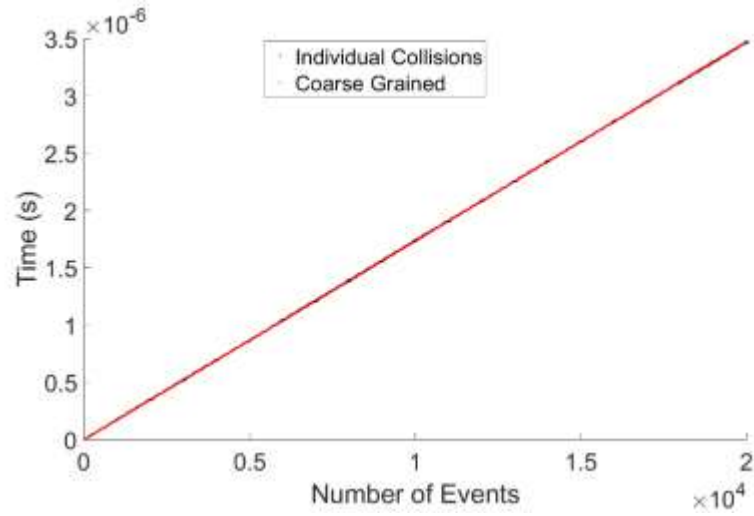


Figure 4-4: Total flight time when individual Collisions are considered against Coarse Grained Model on electric fields and start times with $m=20,000$ events, $E=55$ N/C.

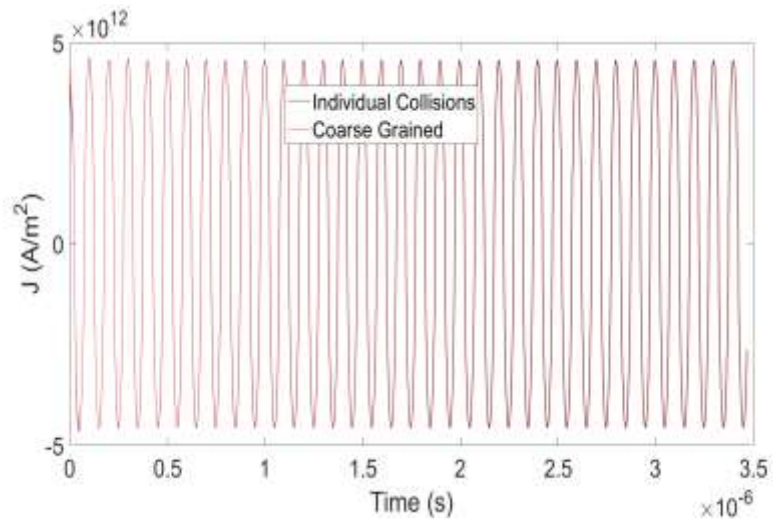


Figure 4-5: Current Density of individual Collisions against Coarse Grained Model on electric fields and start times with $m=20,000$ events, $E_0 = 55$ N/C.

Table 4-6: *Individual Collisions (IC) and Coarse-Grained (CG) Model Average Collision Time (τ) for 500 and 20000 Events, $E_0=55$ N/C*

| # Events | τ_{IC} (s) | τ_{CG} (s) | % Difference |
|----------|-------------------------|-------------------------|--------------|
| 500 | 3.593×10^{-11} | 3.571×10^{-11} | 0.62% |
| 20,000 | 3.465×10^{-11} | 3.469×10^{-11} | 0.11% |

Table 4-7: *Individual Collisions and Coarse-Grained Models' Current Density (J_{rms}) for 500 and 20000 Events, $E_0=55$ N/C*

| # Events | $J_{rms_{IC}}$ (A/m^2) | $J_{rms_{CG}}$ (A/m^2) | % Difference |
|----------|----------------------------|----------------------------|--------------|
| 500 | 3.344×10^{12} | 3.323×10^{12} | 0.62% |
| 20,000 | 3.223×10^{12} | 3.223×10^{12} | 0.11% |

The results shown in Figure 4-2 to Figure 4-4 and Table 4-6 and Table 4-7 indicate that the homotopy model agrees in general with the full simulation values for an electric field of 55 N/C. Additionally, the estimated error decreases as the number of events increases, as seen in the total flight time vs number of events (Figure 4-2 and Figure 4-4). This shows that the homotopy in two dimensions converges. The same holds true for the average collision time and peak current density. In that regard, the next step, as outlined in the following section, is to verify the accuracy of the model on previously unseen data.

4.2 Model Validation

The results illustrated in Section 4.1 indicate that the homotopy in two dimensions is relatively accurate with input values that were used to construct the model. This section will use the data split to validate the model. The homotopy functions obtained by using the results for the nine electric fields listed in Table 4-1 (minus 10 N/C) were evaluated at

electric fields of 25, 30, and 60 N/C, which were not used to fit the parameters. Tabulated details for other electric fields are viewable in Table 4-8 and Table 4-9. The start times for these simulations were randomized. Event sizes of $m=500$ and $m=20,000$ are shown for electric fields of 30 N/C and 60 N/C. A longer simulation for $m=100,000$ with an electric field of 30 N/C is also illustrated.

Table 4-8: *Comparison of Simulation Output for 2-D Homotopy Average Collision Time for Individual Collisions (IC) and Coarse-Grained (CG) Model*

| E_0 (N/C) | τ_{IC} (s) | τ_{CG} (s) | % Difference |
|-------------|-------------------------|-------------------------|--------------|
| 25 | 5.147×10^{-11} | 5.092×10^{-11} | 1.1% |
| 30 | 4.692×10^{-11} | 4.696×10^{-11} | 0.1% |
| 45 | 3.601×10^{-11} | 3.615×10^{-11} | 0.4% |
| 51 | 3.465×10^{-11} | 3.468×10^{-11} | 0.1% |
| 60 | 3.303×10^{-11} | 3.296×10^{-11} | 0.2% |

Table 4-9: *Comparison of Simulation Output for 2-D Homotopy Peak Current Density*

| E_0 (N/C) | J_{rmsIC} (A/m^2) | J_{rmsCG} (A/m^2) | % Difference |
|-------------|-------------------------|-------------------------|--------------|
| 25 | 2.177×10^{12} | 9.091×10^{12} | 1.1% |
| 30 | 2.381×10^{12} | 2.384×10^{12} | 0.1% |
| 45 | 2.742×10^{12} | 2.752×10^{12} | 0.4% |
| 51 | 2.990×10^{12} | 2.992×10^{12} | 0.1% |
| 60 | 3.353×10^{12} | 3.350×10^{12} | 0.2% |

Figure 4-6 to Figure 4-11 presents the results of simulations comparing individual collisions with a coarse-grained model. In all cases, the results are similar to those illustrated in section 4.1.2. The values for the total flight time, average collision time, and

current density in the coarse-grained model converge toward the real value. Additionally, Figure 4-10 shows that even for a number of events greater than 20,000, the model remains relatively consistent.

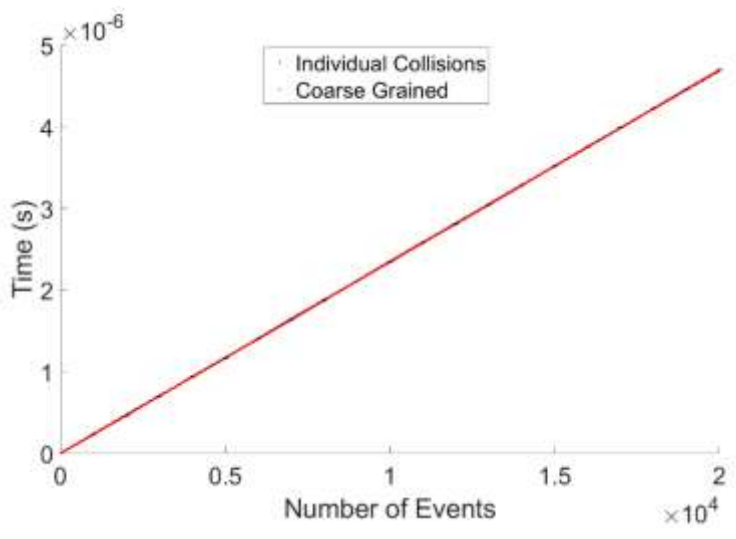


Figure 4-6: Total Flight Time of individual Collisions against Coarse Grained Model on electric fields and start times with $m=20,000$ events, $E=30$ N/C.

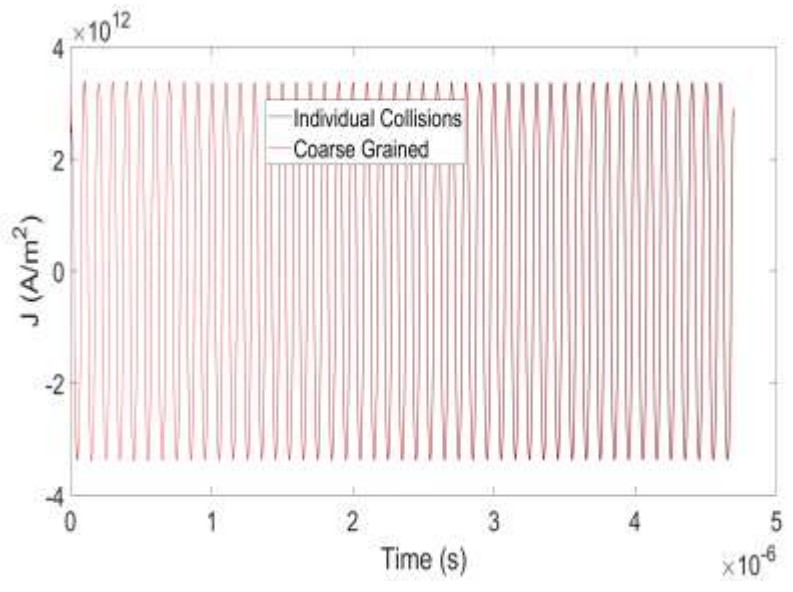


Figure 4-7: Current density of individual Collisions against Coarse Grained Model on electric fields and start times with $m=20,000$ events, $E=30$ N/C.

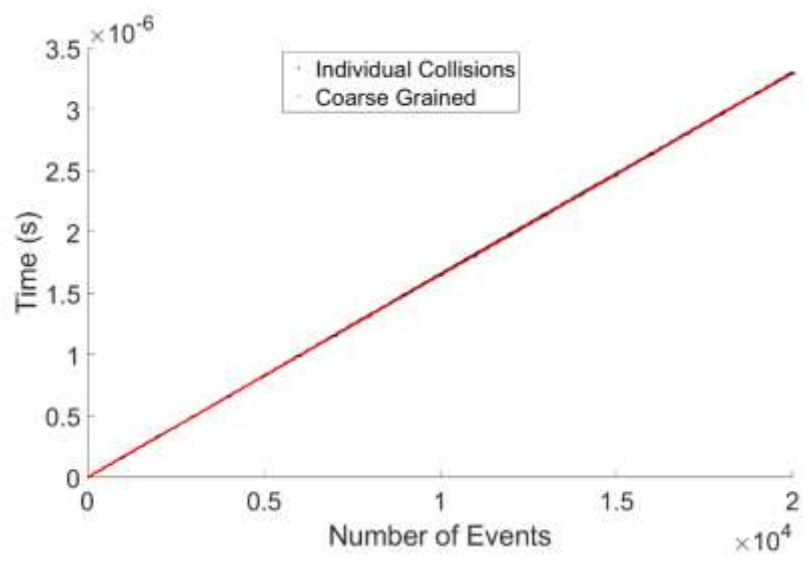


Figure 4-8: Total Flight time of individual Collisions against Coarse Grained Model on electric fields and start times with $m=20,000$ events, $E=60$ N/C.

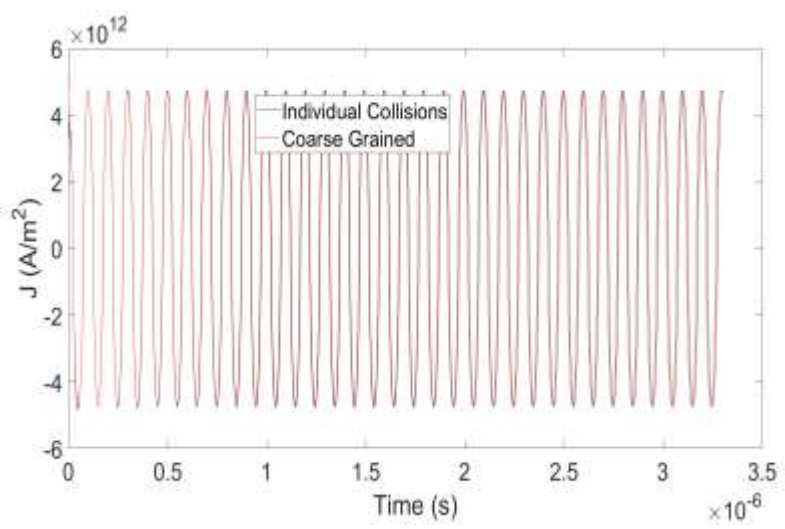


Figure 4-9: Current density of individual Collisions against Coarse Grained Model on electric fields and start times with $m=20,000$ events, $E=60$ N/C.

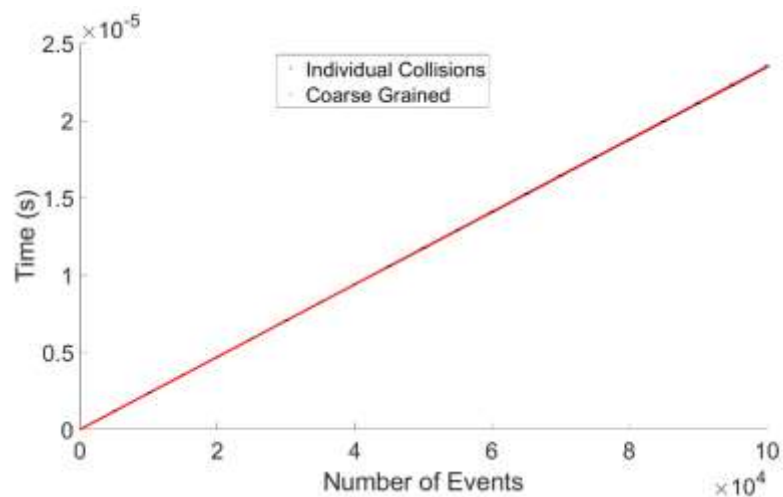


Figure 4-10: Total Flight time of individual Collisions against Coarse Grained Model on electric fields and start times with $m=100,000$ events, $E=30$ N/C.

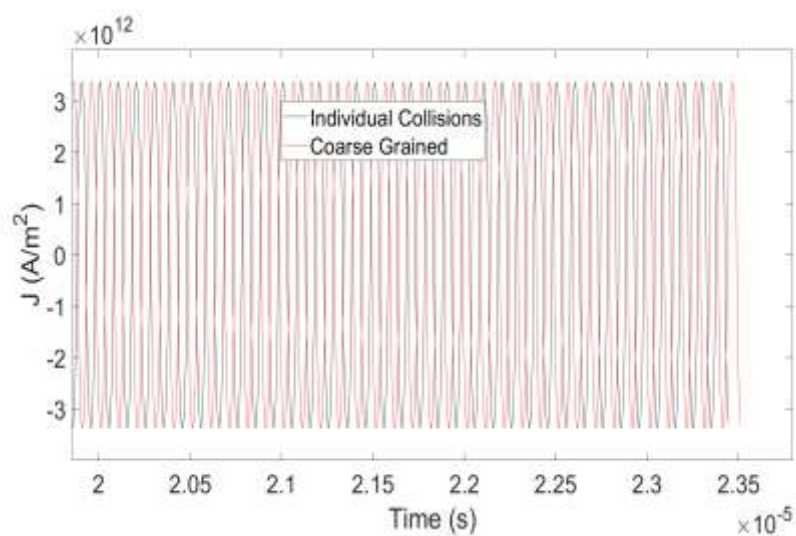


Figure 4-11: Current density of individual Collisions against Coarse Grained Model on electric fields and start times with $m=100,000$ events, $E=30$ N/C.

Furthermore, Table 4-8 highlights the percentage difference between the simulations at $m=20000$ for the test data sets. The model, as shown in Table 4-8, is accurate to less than 0.2% when compared with actual results for all output parameters. This indicates that the model that has been coarse-grained via a homotopy is both valid and accurate for input values within its range. Regardless of start time or electric field,

the model is able to accurately predict the flight time of a group of collisions of $n=5$.

Also, the model can further be coarse-grained where events are further grouped together, that is, with n being some multiple of 5 using the current model. In such a case, there is no resultant reduction in model accuracy as the number of values sorted increases.

One area where the presented work has been untested is on the extremes of electric field ($15 \leq E_0 < 25$ and $85 \leq E_0 < 100$), which is near the minimum and maximum values. In such areas, the model was not fully examined with unseen data that was not used in building the model.

While the model performance within the listed range was good, performance at these extrema was not evaluated. Another limitation is that extrapolation is not possible as the model is limited to only the set interval in electric fields presented. Investigations of the model showed that outside of the specified range, the model diverges greatly (Figure 4-12 and Figure 4-13). With this in mind, a further look at these points is needed and is discussed in the future plans section of this work.

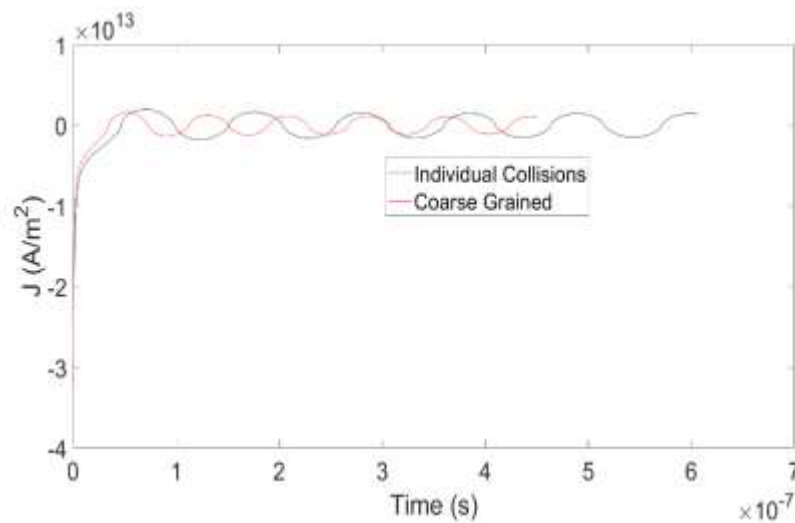


Figure 4-12: Current density of individual Collisions against Coarse Grained Model on electric fields and start times with $m=1000$ events, $E_0=5$ N/C.

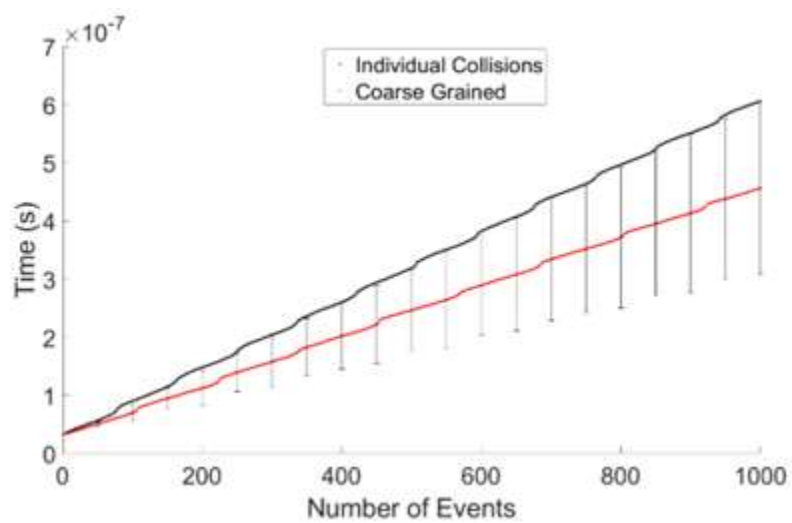


Figure 4-13: Total Flight Time of individual Collisions against Coarse Grained Model on electric fields and start times with $m=1000$ events, $E_0=5$ N/C.

CHAPTER 5

OTHER TECHNIQUES AND METHODS

5.1 Homotopy on Position

In the process of developing the model presented above, a number of techniques and methods were evaluated. These methods were either inadequate or inaccurate or were simply too complicated and were discarded in favor of the one presented in Chapters 3 and 4. The following highlights some of these methods as well as some additional techniques that were evaluated during the course of this work. These are included here as evidence of lessons learned but also as an acknowledgment that these may be valid options for similar applications.

Section 2.3 highlighted the overall methodology used in this work. While the model that was selected uses the start time, a homotopy on start position was also attempted. The idea was to generate a distribution probability for the position of a charge carrier after n collisions (1 event) based on the carrier's start position as opposed to a distribution of time of flight from the carrier start time. This was attempted first because the position in space is more intuitive than a “position” in time space. Similar data was generated for groups of $n=5$ collisions and repeated up to $m=10,000$ times. Initial analysis of the shape of the histogram representing this data for a single combination of input parameters indicated that the data likely followed a generalized beta distribution. The probability density function for the beta distribution is given by:

$$f(x; a, b, \alpha, \beta) = \frac{\Gamma(\alpha+\beta)}{\Gamma(\alpha)\Gamma(\beta)} \frac{(x-a)^{\alpha-1}(b-x)^{\beta-1}}{(b-a)^{\alpha+\beta-2}}, a \leq x \leq b; \alpha, \beta > 0 \quad \text{Eq. 5-1}$$

In Eq. 5-1, a and b represent the minimum and maximum of the dataset, respectively, while α and β are the shape parameters that describe the shape of the distribution. One of the strengths of the beta distribution is that it can describe distributions with a non-zero skewness. The generalized beta distribution PDF is also able to represent all real values (positive and negative); therefore, it was selected, and the plots are shown in Figure 5-1.

Figure 5-1 and Table 5-1 outline the data and parameter estimates, respectively, for the displacement after one event. From Figure 5-2, it can be seen that c) and d) are very similar. Despite this similarity in shape, the parameters representing the distributions are very different. Data generated using the parameter estimates are very similar to those of the individual collision data. The similarity scores in Table 5-1 indicate that apart from $m=100$, all other values of m give a similarity score of over 85%. This is clear from Figure 5-2 and Figure 5-3. To further evaluate how well they represented the data, a total of 100,000 data points were generated using the fit parameters in Table 5-1 for each value of m . The resulting data were then plotted and overlaid on the individual collision data for comparison.

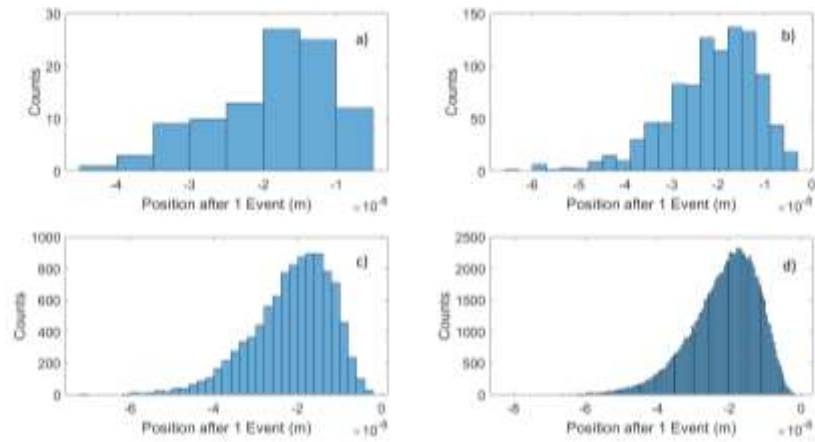


Figure 5-1: Comparison of distributions with varying total number of events (m) describing position data a) 100 events b) 1,000 events c) 10,000 events d) 100,000 events.

Table 5-1: Parameter Estimates and Similarity for Varying Repetitions Event Sizes

| Size (m) | a | b | α | β | Similarity |
|----------------|-------------------------|-------------------------|----------|---------|------------|
| 100 | -4.040×10^{-8} | -5.330×10^{-9} | 1.8 | 1.161 | 72.00% |
| 1,000 | -6.313×10^{-8} | -3.696×10^{-9} | 4.8 | 2.051 | 85.40% |
| 10,000 | -7.188×10^{-8} | -2.233×10^{-9} | 6.8 | 2.617 | 88.60% |
| 100,000 | -8.216×10^{-8} | -1.494×10^{-9} | 9.1 | 3.010 | 91.47% |

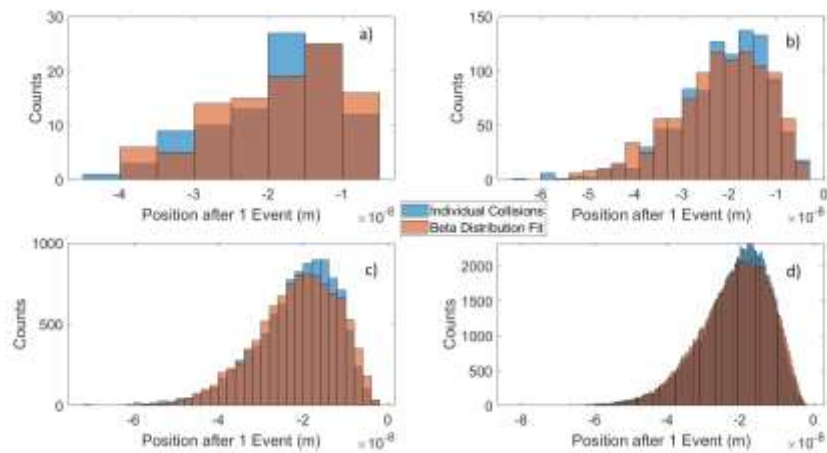


Figure 5-2: Comparison of parameter fit with varying total number of events (m) describing position data a) 100 events b) 1,000 events c) 10,000 events d) 100,000 events.

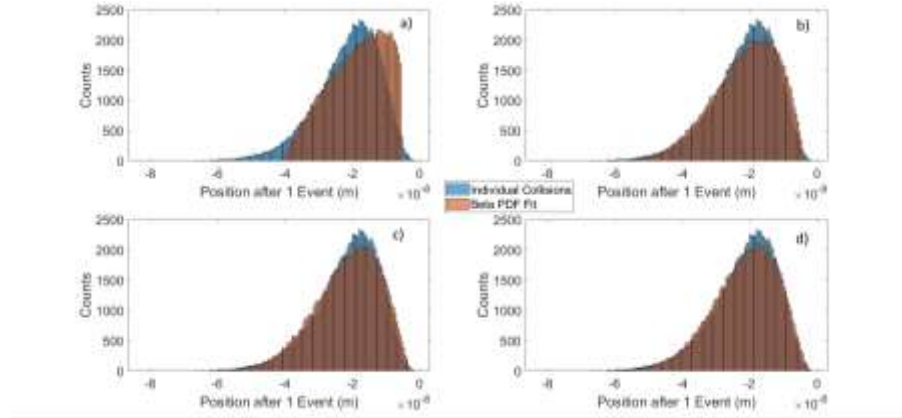


Figure 5-3: Comparison of fit generated from varying total number of events (m) describing position data a) 100 events b) 1,000 events c) 10,000 events d) 100,000 events.

The data presented above indicate that the data can be appropriately modeled with only 10,000 events. This was confirmed by the similarity scores, which were similar to the time data (88.2% at 1,000 events and 90.34% at 10,000 events). These similarity scores were further improved by utilizing an iterative optimization of the beta distribution parameters. One major drawback with attempting to use the beta distribution is that, as discussed above, different values for α and β provide near identical distributions; therefore, it was not always possible to parameterize. To try to address this issue, another distribution, the Weibull distribution, was considered. The Weibull distribution PDF is outlined below.

$$f(x; \alpha, \mu, \gamma) = \frac{\gamma}{\alpha} \left(\frac{x-\mu}{\alpha} \right)^{\gamma-1} e^{-\left(\frac{x-\mu}{\alpha} \right)^{\gamma}}, x \geq \mu; \gamma, \alpha > 0 \quad \text{Eq. 5-2}$$

In equation 5.2, μ is the location parameter, γ the shape parameter, and α the scale parameter. The parameters representing the distribution across multiple start positions were collected and analyzed for any possible curve fit. A fit was possible in μ , but the other two parameters, α , and γ , did not change in any predictable manner; that is, there was no established pattern within the data. Curve fitting tools such as the MATLAB

curve fitting toolbox and statistical and analysis toolbox were utilized to assist in this venture. However, only non-parametric distributions were fit with an acceptable degree of accuracy. In that regard, the homotopy on start position failed and could not be properly implemented as often no reliable parameters were found during the fitting process.

5.2 Homotopy on Frequency

In addition to a homotopy of start time, a homotopy on frequency was similarly attempted. The details reported here represent the partial completion of this attempt by following a similar methodology to the one outlined in the previous section. Multiple simulations were run with the constant input parameters but varying Frequency and electric field. Table 5-2 outlines the input parameters, and Figure 5-4 shows the analysis of the results.

Table 5-2: *Parameter Estimates and Similarity for Varying Repetitions Event Sizes*

| Parameter | Value |
|--------------------|--|
| E_0 | [10 50 100 500] N/C |
| λ | 4.3×10^{-9} m |
| Time Offset | 0 s |
| Frequency | 1×10^6 to 5×10^{16} Hz |

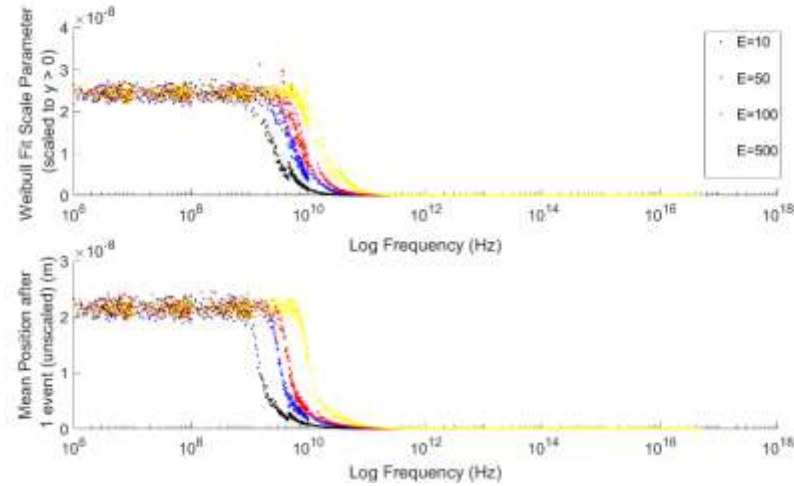


Figure 5-4: Mean position after one event with varied Electric Field and Frequency

Analysis of these simulations indicated that by using the Weibull PDF as outlined in Eq. 5-2, two of the parameters of the Weibull PDF could be predicted, the location and scale parameters. The shape parameter, on the other hand, could not be reliably predicted using this PDF. Values were sporadic and followed no particular trend. Following this set of results, the methodology outlined in Section 3 was the chosen one. The results obtained from these simulations did, however, indicate that homotopy on frequency held promise as the mean position is predictable, as seen in Figure 5-4 but could not be properly curve fit. The outline for this will be discussed in Chapter 6.

CHAPTER 6

CONCLUSIONS AND FUTURE WORK

6.1 Conclusions

A stochastic approach was taken to model charge transport in periodic electric fields by the development of a homotopy on start time and electric field. A total number of collisions as large as 500,000 have been modeled to build this homotopy. This was done to ensure that the presented model was able to scale at an acceptable level with minimal error propagation. This shows the capability of the model to coarse grain charge transport at a nanoscopic resolution while presenting transport properties such as current density in an accurate manner. The results presented here see a quantitative agreement with the original non-coarse grained simulations, and predictions from the model are quantitatively sound on the relationship between various electric fields and current density.

The full model and the parameters needed to replicate it are outlined in Table 4-3 to Table 4-5 and in Eq. 4-1 to Eq. 4-5. Two dimensions are included in this homotopy; start time and electric field. Start times at any point within a cycle and Electric fields within the 15 N/C to 100 N/C range can be represented. The results presented here were obtained for a frequency $\nu = 1 \times 10^7 \text{ Hz}$ and a mean free path $\lambda = 4.3 \times 10^{-9}$. The approach followed here can be used for other frequencies, but it needs to be parameterized for those frequencies. If a third dimension is added, such that parameters

are also a function of the frequency, the model will become more general, but this seems to be a tall order at this time. The presented model can be used as a basis for coarse-graining other transport models using a similar methodology.

Qualitatively, results from the coarse-grained simulations show very good agreements with individual collision simulations. The model accurately predicts peak current density to within 1% or less when a small grain ($n=5$) for larger grains, the accuracy decreases, but it was found to be less than 2% for $n=50$. It is important to clarify that the largest gain in simulation time came from using PDFs to determine the time of flight instead of explicitly evaluating the transport equations, indeed. This work lays the groundwork for further studies on developing a coarse-grained model for charge transport using homotopies. This study can be used as a basis for further development in the frequency domain with time-dependent electric fields.

It is evident from the work that the electric field affects the total flight time of a charge carrier, and that effect can be reliably predicted. Using the distributions and the resultant parameters that were generated, this work has shown that graining in multiple dimensions is possible, and transport properties can be appropriately evaluated.

6.2 Future Work

While the presented model does coarse-grain the charge transport model, there are a few components of the model that need to be further studied. Improvements can be made in the range of electric fields that can be handled by the model. Currently, the limit is limited to 15 N/C to 100 N/C, which is a relatively small range. Larger electric fields of up to 10,000 N/C need to be evaluated and included in the model. Furthermore, much smaller electric fields are also of interest; that is, those below 15 N/C, and indeed

significantly smaller than 1 N/C. Extension of these areas would make the model more broadly applicable and more practically useful.

Another important area of interest is in extending the model to a third dimension; that of frequency. This is of particular importance as the transport properties are being investigated under the effects of a periodic electric field. Said field is directly affected by the frequency. Results highlighted in Chapter 5 indicate that extension into this field is possible; however, preliminary attempts were met with failure. Provided that the proper fitting mechanism can be identified, extension into the frequency domain would be of the utmost importance and relevance as otherwise, the whole process of parametrization will have to be conducted at each frequency.

REFERENCES

- [1] S. Althaf and C. W. Babbitt, “Disruption risks to material supply chains in the electronics sector,” *Resour. Conserv. Recycl.*, vol. 167, p. 105248, Apr. 2021, doi: 10.1016/J.RESCONREC.2020.105248.
- [2] K. Lawrence, “‘Chipageddon’: What the Global Chip Drought Means for Manufacturing and Supply Chains,” *“Chipageddon” What Glob. Chip Drought Means Manuf. Supply Chain.*, Aug. 2021, doi: 10.4135/9781529789683.
- [3] S. K. Paul, P. Chowdhury, M. T. Chowdhury, R. K. Chakraborty, and M. A. Moktadir, “Operational challenges during a pandemic: an investigation in the electronics industry,” *Int. J. Logist. Manag.*, vol. ahead-of-print, no. ahead-of-print, 2021, doi: 10.1108/IJLM-05-2021-0307/FULL/XML.
- [4] M. M. S. Sodhi, “Managing Demand Risk in Tactical Supply Chain Planning for a Global Consumer Electronics Company,” *Prod. Oper. Manag.*, vol. 14, no. 1, pp. 69–79, Mar. 2005, doi: 10.1111/J.1937-5956.2005.TB00010.X.
- [5] SIA, “Chipping In: The positive Impact of The Semiconductor Industry on The American Workforce and How Federal Industry Incentives Will Increase Domestic Jobs,” May 2021. Accessed: May 31, 2022. [Online]. Available: https://www.semiconductors.org/wp-content/uploads/2021/05/SIA-Impact_May2021-FINAL-May-19-2021_2.pdf.
- [6] K. Lawrence, *“Chipageddon”: What the Global Chip Drought Means for Manufacturing and Supply Chains.* 2021.
- [7] F. Yinug, “Semiconductor Shortage Highlights Need to Strengthen U.S. Chip Manufacturing, Research - Semiconductor Industry Association,” Washington, Feb. 2021. Accessed: May 31, 2022. [Online]. Available: <https://www.semiconductors.org/semiconductor-shortage-highlights-need-to-strengthen-u-s-chip-manufacturing-research/>.
- [8] J. Voas, N. Kshetri, and J. F. Defranco, “Scarcity and Global Insecurity: The Semiconductor Shortage,” *IT Prof.*, vol. 23, no. 5, pp. 78–82, 2021, doi: 10.1109/MITP.2021.3105248.
- [9] S. M. Rothrock, “Coronavirus, chip boom, and supply shortage: The new normal for global semiconductor manufacturing,” *Int. Symp. Microelectron.*, vol. 2021, no. 1, pp. 000026–000030, Oct. 2021, doi: 10.4071/1085-8024-2021.1.000026.

- [10] L. de Vos *et al.*, “An Analysis on the Crisis of ‘Chips shortage’ in Automobile Industry -Based on the Double Influence of COVID-19 and Trade Friction,” *J. Phys. Conf. Ser.*, vol. 1971, no. 1, p. 012100, Jul. 2021, doi: 10.1088/1742-6596/1971/1/012100.
- [11] Z. Sai, “Korea and Japan trade friction and its impact on China’s semiconductor industry ,” *Korea Industrial Economics Association*, Nov. 2019. <https://www.dbpia.co.kr/Journal/articleDetail?nodeId=NODE09314267> (accessed Jun. 20, 2022).
- [12] Y.-H. Chu, S.-M. Hsu, C.-C. Chang, and S.-H. Hsu, “An Economy-wide Impact Assessment of US-China Trade Friction on Taiwan’s Semiconductor Industry,” Apr. 2019, Accessed: Jun. 20, 2022. [Online]. Available: https://www.gtapp.agecon.purdue.edu/resources/res_display.asp?RecordID=5818.
- [13] N. Kamakura, “From globalising to regionalising to reshoring value chains? The case of Japan’s semiconductor industry,” *Cambridge J. Reg. Econ. Soc.*, vol. 15, no. 2, pp. 261–277, Jun. 2022, doi: 10.1093/CJRES/RSAC010.
- [14] J. Wen, “The Impact of Sino-US Trade War on Volatility Spillover Effect Between Related Industries in Sino-US Stock Market,” *7th Int. Conf. Financ. Innov. Econ. Dev.*, pp. 1590–1602, Mar. 2022, doi: 10.2991/AEBMR.K.220307.260.
- [15] “Senate approved \$52 billion in subsidies for chip manufacturing,” *The Washington Post*, Jun. 14, 2021.
- [16] The White House, Department of Commerce, Department of Energy, Department of Defense, and Department of Health and Human Services, “Building Resilient Supply Chains, Revitalizing American Manufacturing, And Fostering Broad-Based Growth,” Washington, Jun. 2021.
- [17] C. S. S. Sangeeth, P. Jiménez, A. M. Benito, W. K. Maser, and R. Menon, “Charge transport properties of water dispersible multiwall carbon nanotube-polyaniline composites,” *J. Appl. Phys.*, vol. 107, no. 10, 2010, doi: 10.1063/1.3374628.
- [18] P. Maniadis, G. Kalosakas, K. Rasmussen, and A. R. Bishop, “Ac conductivity in a DNA charge transport model,” *Phys. Rev. E - Stat. Nonlinear, Soft Matter Phys.*, vol. 72, no. 2, p. 021912, Aug. 2005, doi: 10.1103/PhysRevE.72.021912.
- [19] C. Leon and J. Santamaria, “Defects, impurities, and transport phenomenon in oxide crystals,” *Ep. Growth Complex Met. Oxides*, pp. 209–229, Jan. 2015, doi: 10.1016/B978-1-78242-245-7.00008-7.
- [20] R. Ma *et al.*, “Direct Four-Probe Measurement of Grain-Boundary Resistivity and Mobility in Millimeter-Sized Graphene,” *Nano Lett.*, vol. 17, no. 9, pp. 5291–5296, Sep. 2017, doi: 10.1021/ACS.NANOLETT.7B01624/SUPPL_FILE/NL7B01624_SI_001.PDF.

- [21] A. Kokil, K. Yang, and J. Kumar, "Techniques for characterization of charge carrier mobility in organic semiconductors," *J. Polym. Sci. Part B Polym. Phys.*, vol. 50, no. 15, pp. 1130–1144, Aug. 2012, doi: 10.1002/polb.23103.
- [22] O. Hilt and L. D. A. Siebbeles, "Time and frequency dependent charge carrier mobility of one-dimensional chains with energetic disorder," *Chem. Phys. Lett.*, vol. 269, no. 3–4, pp. 257–262, May 1997, doi: 10.1016/S0009-2614(97)00274-1.
- [23] R. Coehoorn, W. F. Pasveer, P. A. Bobbert, and M. A. J. Michels, "Charge-carrier concentration dependence of the hopping mobility in organic materials with Gaussian disorder," *Phys. Rev. B - Condens. Matter Mater. Phys.*, vol. 72, no. 15, p. 155206, Oct. 2005, doi: 10.1103/PhysRevB.72.155206.
- [24] I. I. Fishchuk, A. Kadashchuk, and H. Bässler, "Theory of hopping charge-carrier transport at large carrier concentrations in disordered organic solids: Polarons versus bare charge carriers," in *Physica Status Solidi (C) Current Topics in Solid State Physics*, Jul. 2008, vol. 5, no. 3, pp. 746–749, doi: 10.1002/pssc.200777558.
- [25] E. F. Hairetdinov and N. F. Uvarov, "Estimation of the charge carrier concentration in NaCl single crystals from analysis of the frequency dependent conductivity," *Solid State Ionics*, vol. 136–137, pp. 967–970, Nov. 2000, doi: 10.1016/S0167-2738(00)00513-0.
- [26] C. Tanase, E. J. Meijer, P. W. M. Blom, and D. M. De Leeuw, "Local charge carrier mobility in disordered organic field-effect transistors," *Org. Electron.*, vol. 4, no. 1, pp. 33–37, Jun. 2003, doi: 10.1016/S1566-1199(03)00006-5.
- [27] V. Podzorov, S. E. Sysoev, E. Loginova, V. M. Pudalov, and M. E. Gershenson, "Single-crystal organic field effect transistors with the hole mobility ~ 8 cm²/Vs," *Appl. Phys. Lett.*, vol. 83, no. 17, p. 3504, Oct. 2003, doi: 10.1063/1.1622799.
- [28] C. S. S. Sangeeth, M. Jaiswal, and R. Menon, "Charge transport in transparent conductors: A comparison," *J. Appl. Phys.*, vol. 105, no. 6, p. 063713, Mar. 2009, doi: 10.1063/1.3097759.
- [29] Z. Bao, A. J. Lovinger, and A. Dodabalapur, "Organic field-effect transistors with high mobility based on copper phthalocyanine," *Appl. Phys. Lett.*, vol. 69, no. 20, p. 3066, Jun. 1998, doi: 10.1063/1.116841.
- [30] H. Luo *et al.*, "Remarkable enhancement of charge carrier mobility of conjugated polymer field-effect transistors upon incorporating an ionic additive," *Sci. Adv.*, vol. 2, no. 5, May 2016, doi: 10.1126/SCIADV.1600076/SUPPL_FILE/1600076_SM.PDF.
- [31] E. J. Meijer, C. Detcheverry, P. J. Baesjou, E. Van Veenendaal, D. M. De Leeuw, and T. M. Klapwijk, "Dopant density determination in disordered organic field-effect transistors," *J. Appl. Phys.*, vol. 93, no. 8, p. 4831, Mar. 2003, doi: 10.1063/1.1559933.

- [32] Y. Chen, G. M. Smith, E. Loughman, Y. Li, W. Nie, and D. L. Carroll, "Effect of multi-walled carbon nanotubes on electron injection and charge generation in AC field-induced polymer electroluminescence," *Org. Electron.*, vol. 14, no. 1, pp. 8–18, Jan. 2013, doi: 10.1016/J.ORGEL.2012.10.017.
- [33] M. C. Vecchi and M. Rudan, "Modeling electron and hole transport with full-band structure effects by means of the spherical-harmonics expansion of the BTE," *IEEE Trans. Electron Devices*, vol. 45, no. 1, pp. 230–238, 1998, doi: 10.1109/16.658836.
- [34] D. Chen, E. C. Kan, U. Ravaioli, C. W. Shu, and R. W. Dutton, "An Improved Energy Transport Model Including Nonparabolicity and Non-Maxwellian Distribution Effects," *IEEE Electron Device Lett.*, vol. 13, no. 1, pp. 26–28, 1992, doi: 10.1109/55.144940.
- [35] A. Majorana, O. Muscato, and C. Milazzo, "Charge transport in 1D silicon devices via Monte Carlo simulation and Boltzmann-Poisson solver," *COMPEL - Int. J. Comput. Math. Electr. Electron. Eng.*, vol. 23, no. 2, pp. 410–425, 2004, doi: 10.1108/03321640410510578/FULL/XML.
- [36] C. Jacoboni and L. Reggiani, "The Monte Carlo method for the solution of charge transport in semiconductors with applications to covalent materials," *Rev. Mod. Phys.*, vol. 55, no. 3, pp. 645–705, Jul. 1983, doi: 10.1103/RevModPhys.55.645.
- [37] K. Shimakawa and S. Kasap, "Dynamics of Carrier Transport in Nanoscale Materials: Origin of Non-Drude Behavior in the Terahertz Frequency Range," *Appl. Sci. 2016, Vol. 6, Page 50*, vol. 6, no. 2, p. 50, Feb. 2016, doi: 10.3390/APP6020050.
- [38] P. Di Sia, "An analytical transport model for nanomaterials," *J. Comput. Theor. Nanosci.*, vol. 8, no. 1, pp. 84–89, Jan. 2011, doi: 10.1166/JCTN.2011.1663.
- [39] T. L. Cocker *et al.*, "Microscopic origin of the Drude-Smith model," *Phys. Rev. B*, vol. 96, no. 20, p. 205439, Nov. 2017, doi: 10.1103/PHYSREVB.96.205439/FIGURES/8/MEDIUM.
- [40] J. W. Jerome, *Analysis of Charge Transport*. Springer Berlin Heidelberg, 1996.
- [41] A. M. Johansen, "Monte Carlo Methods," *Int. Encycl. Educ.*, pp. 296–303, Jan. 2010, doi: 10.1016/B978-0-08-044894-7.01543-8.
- [42] R. O. Grondin, S. M. El-Ghazaly, and S. Goodnick, "A review of global modeling of charge transport in semiconductors and full-wave electromagnetics," *IEEE Trans. Microw. Theory Tech.*, vol. 47, no. 6 PART 2, pp. 817–829, 1999, doi: 10.1109/22.769315.
- [43] V. Tozzini, "Coarse-grained models for proteins," *Curr. Opin. Struct. Biol.*, vol. 15, no. 2, pp. 144–150, Apr. 2005, doi: 10.1016/J.SBI.2005.02.005.

- [44] E. Brini, E. A. Algaer, P. Ganguly, C. Li, F. Rodríguez-Roperero, and N. F. A. Van Der Vegt, “Systematic coarse-graining methods for soft matter simulations – a review,” *Soft Matter*, vol. 9, no. 7, pp. 2108–2119, Jul. 2013, doi: 10.1039/C2SM27201F.
- [45] W. G. Noid *et al.*, “The multiscale coarse-graining method. I. A rigorous bridge between atomistic and coarse-grained models,” *J. Chem. Phys.*, vol. 128, no. 24, p. 244114, Jun. 2008, doi: 10.1063/1.2938860.
- [46] S. Izvekov and G. A. Voth, “A multiscale coarse-graining method for biomolecular systems,” *J. Phys. Chem. B*, vol. 109, no. 7, pp. 2469–2473, Feb. 2005, doi: 10.1021/JP044629Q/SUPPL_FILE/JP044629QSI20041124_112603.PDF.
- [47] N. E. Jackson, “Coarse-Graining Organic Semiconductors: The Path to Multiscale Design,” *J. Phys. Chem. B*, vol. 125, no. 2, pp. 485–496, Jan. 2020, doi: 10.1021/ACS.JPCB.0C09749.
- [48] E. A. Oprzeska-Zingrebe and J. Smiatek, “Some Notes on the Thermodynamic Accuracy of Coarse-Grained Models,” *Front. Mol. Biosci.*, vol. 6, p. 87, Sep. 2019, doi: 10.3389/FMOLB.2019.00087/BIBTEX.
- [49] H. Wang, C. Junghans, and K. Kremer, “Comparative atomistic and coarse-grained study of water: What do we lose by coarse-graining?,” *Eur. Phys. J. E* 2009 282, vol. 28, no. 2, pp. 221–229, Jan. 2009, doi: 10.1140/EPJE/I2008-10413-5.
- [50] T. Kubař and M. Elstner, “Coarse-grained time-dependent density functional simulation of charge transfer in complex systems: Application to hole transfer in DNA,” *J. Phys. Chem. B*, vol. 114, no. 34, pp. 11221–11240, Sep. 2010, doi: 10.1021/JP102814P/SUPPL_FILE/JP102814P_SI_001.PDF.
- [51] Z. J. Wang and M. Deserno, “A systematically coarse-grained solvent-free model for quantitative phospholipid bilayer simulations,” *J. Phys. Chem. B*, vol. 114, no. 34, pp. 11207–11220, Sep. 2010, doi: 10.1021/JP102543J.
- [52] M. Attarian Shandiz, F. Salvat, and R. Gauvin, “Detailed Monte Carlo Simulation of electron transport and electron energy loss spectra,” *Scanning*, vol. 38, no. 6, pp. 475–491, Nov. 2016, doi: 10.1002/SCA.21280.
- [53] N. Harada, Y. Awano, S. Sato, and N. Yokoyama, “Monte Carlo simulation of electron transport in a graphene diode with a linear energy band dispersion,” *J. Appl. Phys.*, vol. 109, no. 10, p. 104509, May 2011, doi: 10.1063/1.3581118.
- [54] B. Gelmont, K. Kim, and M. Shur, “Monte Carlo simulation of electron transport in gallium nitride,” *J. Appl. Phys.*, vol. 74, no. 3, p. 1818, Jun. 1998, doi: 10.1063/1.354787.
- [55] J. Singh, *Modern Physics for Engineers*, 1st ed. Wiley, 1999.

- [56] A. C. Sparavigna, “The Boltzmann Equation Of Phonon Thermal Transport Solved In the Relaxation Time Approximation – I – Theory,” *Mech. Mater. Sci. Eng. J.*, vol. 2016, no. 3, pp. 34–45, 2016, doi: 10.13140/RG.2.1.1001.1923.
- [57] J.-P. M. Péraud, C. D. Landon, and N. G. Hadjiconstantinou, “Monte Carlo methods for solving the Boltzmann equation,” in *Annual Review of Heat Transfer*, Begell House, Inc., 2014, pp. 205–266.
- [58] T. T. Bramlette and R. H. Mallett, “A finite element solution technique for the Boltzmann equation,” *J. Fluid Mech.*, vol. 42, no. 1, pp. 177–191, Jun. 1970, doi: 10.1017/S0022112070001167.
- [59] N. Singh, “Electronic transport theories from simple to strange metals: A summary,” in *Electronic Transport Theories: From Weakly to Strongly Correlated Materials*, CRC Press, 2016, pp. 1–213.
- [60] “The Drude Model of Metals.” Accessed: Feb. 07, 2022. [Online]. Available: https://www.doitpoms.ac.uk/tlplib/thermal_electrical/drude.php.
- [61] M. S. Wartak and C.-Y. Fong, “Free-Electron Approximation,” <https://doi.org/10.1117/3.2510243.ch18>, vol. FG43, pp. 18–19, Jan. 2019, doi: 10.1117/3.2510243.CH18.
- [62] W. Brütting, W. Rieß, and M. Schwoerer, “DC Conductivity and Peierls instability in the quasi-one-dimensional organic charge density wave conductor (fluoranthene)₂X,” *Ann. Phys.*, vol. 504, no. 6, pp. 409–422, Jan. 1992, doi: 10.1002/andp.19925040604.
- [63] W. Rieß and W. Briitting, “Charge density waves in organic conductors: (fluoranthene)₂x as a model system,” *Phys. Scr.*, vol. 1993, no. T49B, pp. 721–725, Jan. 1993, doi: 10.1088/0031-8949/1993/T49B/058.
- [64] X. Zhang, F. Wang, A. Li, and W. Fan, “An Improved Fluid Model Study: The Effect of Cross-Section Geometry on Positive Corona Discharge on DC Transmission Conductors,” *IEEE Trans. Plasma Sci.*, vol. 48, no. 8, pp. 2846–2855, Aug. 2020, doi: 10.1109/TPS.2020.3009407.
- [65] L. C. Bourne, M. S. Sherwin, and A. Zettl, “Elastic properties of charge-Density-Wave conductors: Ac-dc electric field coupling,” *Phys. Rev. Lett.*, vol. 56, no. 18, pp. 1952–1955, May 1986, doi: 10.1103/PhysRevLett.56.1952.
- [66] J. Ma *et al.*, “Impact of Stabilizer Layers on the Thermal-Electromagnetic Characteristics of Direct Current Carrying HTS Coated Conductors under Perpendicular AC Magnetic Fields,” *IEEE Trans. Appl. Supercond.*, vol. 30, no. 4, Jun. 2020, doi: 10.1109/TASC.2020.2977004.

- [67] S. S. Rekhviashvili and A. A. Alikhanov, "Simulation of drift-diffusion transport of charge carriers in semiconductor layers with a fractal structure in an alternating electric field," *Semicond. 2017 516*, vol. 51, no. 6, pp. 755–759, Jun. 2017, doi: 10.1134/S1063782617060264.
- [68] N. Karl, "Charge carrier transport in organic semiconductors," *Synth. Met.*, vol. 133–134, pp. 649–657, Mar. 2003, doi: 10.1016/S0379-6779(02)00398-3.
- [69] S. Suhai, "Charge Carrier Mobilities in Periodic DNA Models," *J. Chem. Phys.*, vol. 57, no. 12, p. 5599, Sep. 2003, doi: 10.1063/1.1678261.
- [70] D. J. Bergman and Y. M. Strelniker, "Anisotropic ac Electrical Permittivity of a Periodic Metal-Dielectric Composite Film in a Strong Magnetic Field," *Phys. Rev. Lett.*, vol. 80, no. 4, p. 857, Jan. 1998, doi: 10.1103/PhysRevLett.80.857.
- [71] T. A. Driscoll, N. Hale, and L. N. Trefethen, *Chebfun Guide*. Oxford: Pafnuty Publications, 2014.
- [72] P. Maniadis, G. Kalosakas, K. Rasmussen, and A. R. Bishop, "Ac conductivity in a DNA charge transport model," *Phys. Rev. E - Stat. Nonlinear, Soft Matter Phys.*, vol. 72, no. 2, 2005, doi: 10.1103/PhysRevE.72.021912.
- [73] C. S. Suchand Sangeeth, R. Kannan, V. K. Pillai, and R. Menon, "Charge transport in functionalized multi-wall carbon nanotube-Nafion composite," in *Journal of Applied Physics*, Sep. 2012, vol. 112, no. 5, p. 053706, doi: 10.1063/1.4749264.
- [74] L. R. Zhou *et al.*, "Study on charge transport mechanism and space charge characteristics of polyimide films," in *IEEE Transactions on Dielectrics and Electrical Insulation*, Aug. 2009, vol. 16, no. 4, pp. 1143–1149, doi: 10.1109/TDEI.2009.5211868.
- [75] C. Zhou and G. Chen, "Space charge and AC electrical breakdown strength in polyethylene," *IEEE Trans. Dielectr. Electr. Insul.*, vol. 24, no. 1, pp. 559–566, Feb. 2017, doi: 10.1109/TDEI.2016.005811.
- [76] D. L. Woolard, H. Tian, R. J. Trew, M. A. Littlejohn, and K. W. Kim, "Hydrodynamic electron-transport model: Nonparabolic corrections to the streaming terms," *Phys. Rev. B*, vol. 44, no. 20, p. 11119, Nov. 1991, doi: 10.1103/PhysRevB.44.11119.
- [77] W. Zhang *et al.*, "Solving the Boltzmann equation to obtain electron transport coefficients and rate coefficients for fluid models," *Plasma Sources Sci. Technol.*, vol. 14, no. 4, p. 722, Oct. 2005, doi: 10.1088/0963-0252/14/4/011.
- [78] T.-D. Bradley, J. Terilla, and T. Bryson, *Topology : A categorical approach*.

- [79] M. Stone, “Cross-Validatory Choice and Assessment of Statistical Predictions,” *J. R. Stat. Soc. Ser. B*, vol. 36, no. 2, pp. 111–133, Jan. 1974, doi: 10.1111/J.2517-6161.1974.TB00994.X.
- [80] P. Refaeilzadeh, L. Tang, and H. Liu, “Cross-Validation,” in *Encyclopedia of Database Systems*, Springer US, 2009, pp. 532–538.